Università degli Studi di Napoli "Federico II"

Facoltà di Ingegneria

Tesi di Dottorato di Ricerca
in
Ingegneria Aerospaziale, Navale e della Qualità
XVIII Ciclo

Analysis and Design of a Multi-phase Catalytic Reactor for the Decomposition of Hydrogen Peroxide in Space Propulsive Systems

Relatori
Ch.mo Prof. Ing. Annamaria Russo Sorge
Ch.mo Prof. Ing. Maria Turco

Candidato
Ing. Salvatore Bonifacio

Coordinatore del Corso di Dottorato
Ch.mo Prof. Ing. Antonio Moccia

Novembre 2006

Anno Accademico 2005/2006

TABLE OF CONTENTS

List of figures

List of tables

NOMENCLATURE

Acronyms:

HTP	:	High Test Peroxide
RCS	:	Reaction Control System
OMS	:	Orbital Manoeuvring System
MEMS	:	Micro Electro-Mechanical System

Symbols:

T	:	temperature [K]
ρ	:	density [kg/m^3]
V	:	velocity [m/s]
h	:	heat transfer coefficient [W/(m^2·K)]
c_p	:	constant-pressure specific heat [J/(kg·K)]
X	:	mole fraction [-]
Y	:	mass fraction [-]
k_d	:	mass transfer coefficient [m/s]
x	:	distance along the monolith channel [m]
t	:	time [s]
M	:	molecular weight [kg/mol]
S	:	surface to volume ratio [m^{-1}]
A_c	:	channel cross section area [m^2]
r_s	:	reaction rate [mol/(m^2·s)]
C	:	concentration [mol/m^3]
A	:	pre-exponential factor [consistent units]
E_a	:	activation energy [J/mol]
R	:	universal gas constant [8.314 J/(mol·K)]
R_{mix}	:	mixture specific gas constant [J/(kg·K)]
P	:	pressure [N/m^2]
μ	:	viscosity [kg/(m·s)]
λ	:	thermal conductivity [W/(m·K)]
D	:	diffusion coefficient [m^2/s]
σ	:	surface tension [N/m]
H	:	Henry constant [-]
r_v	:	volumetric reaction rate [mol/(m^3·s)]
Ω_v	:	viscosity collision integral [-]
σ_s	:	hard-sphere diameter [Angstrom]
k_B	:	Boltzmann constant [1.3806·10^{-23}m^2·kg·s^{-2}·K^{-1}]
ε	:	characteristic energy [m^2·kg·s^{-2}]
T^*	:	dimensionless temperature [-]
c_v	:	constant-volume specific heat [J/(kg·K)]
Ω_d	:	diffusion collision integral [-]
N_{sp}	:	number of species [-]
d_h	:	hydraulic diameter [m]
p	:	channel cross section perimeter [m]
r	:	radial coordinate [m]

x^+	:	non-dimensional axial coordinate (Graetz number) [-]
r^+	:	non-dimensional radial coordinate [m]
u	:	axial velocity [m/s]
u^+	:	non-dimensional axial velocity [m/s]
α	:	thermal diffusivity [m^2/s]
v	:	kinematic viscosity [m^2/s]
Re	:	Reynolds number [-]
Pr	:	Prandlt number [-]
Sc	:	Schmidt number [-]
Le	:	Lewis number [-]
Nu	:	Nusselt number [-]
Sh	:	Sherwood number [-]
θ	:	non dimensional temperature [-]

Superscripts/subscripts:

g	:	gas-phase
w	:	wall (solid-phase)
m	:	mean value across the channel cross section
i	:	species i-th
j	:	species j-th
ref	:	reference temperature
Q	:	constant wall heat flux
T	:	constant wall temperature
in	:	inlet

1. INTRODUCTION

1.1 Scenario

At the beginning of the space age, the environmental impact of rocket engines played virtually no role in decisions affecting their development or use. For launchers boosters, many systems evolving from the German V-2 missile used liquid oxygen and a form of kerosene as oxidizer and fuel. Eventually, engines such as M-1, J-2 and RL-10 replaced the RP-1 kerosene with liquid hydrogen, which was trickier to handle but more powerful in terms of thrust.

Payload yields have been then increased adding solid fuel motors to the rocket's first stages: storable but highly toxic and corrosive liquids have been widely used as fuels and oxidizers in some of the most successful launchers (as the Titan and Delta series).

High performance upper stages and spacecraft thrusters have been almost exclusively based on hydrazine, another difficult to handle liquid fuel.

Environmental effects of space propulsive systems became a factor in 1972 with the first flight of the Space Shuttle [1]. Being the launch site perched on the edge of a wildlife reserve, NASA was concerned that the spacecraft's anticipated high flight rates might damage the flora and the fauna that made the grounds of the Kennedy Space Centre their home. Since then, environmental issues have been taken much more seriously in the development, production and maintenance of rocket propulsion systems, with growing attention also to the impact of engine's exhausts on the atmosphere.

"Green" fuels and oxidizers not only reduce the cost and ease of handling and assembly of the rockets they drive, but might also increase the number of potential launch sites.

The "greening" of rocketry has spread to upper stages and satellite propulsion systems too and designers are considering alternatives to hydrazine-driven thrusters: up to present, rocket propellants as nitrogen, nitrous oxide, butane, water and xenon have been employed. But these "low-end" propellants are not able to attain the same performances of existing engines based on toxic and carcinogenic chemicals as hydrazine and nitrogen tetroxide, hence new propellants and propellants' combinations need to be investigated.

In this framework, highly concentrated solutions of hydrogen peroxide, commonly referred to as high test peroxide (HTP) have been identified as one of the most promising solutions: in the last ten years, HTP-based propulsive systems ranging from future Single Stage To Orbit launchers to micro-satellite's thrusters have been subject of investigation.

7

In the following sections, the advantages related to the utilization of HTP in both high-thrust and low-thrust level applications will be illustrated; then, the most critical issues related to the design of a HTP-based propulsion system will be presented.

1.2 Analysis and trade-off of propellants for space propulsive systems

Hydrogen peroxide is not a new entry in the family of chemicals used for propulsive applications, as it has been widely used since the beginning of the space age: its first application dates back to 1935, when Walter equipped the Henkel 176 with ATO (Assisted Take Off) units fed with a hydrogen peroxide solution (80% weight) [2]. In 1941, the first aircraft powered by a rocket engine, i.e. the Messerschmidt 163, made its first flight, reaching speeds up to 1000km/h, while the most advanced military jets of that time were limited to 600-700km/h: the main engine of the Messerschmidt 163 (a schematic drawing is shown in Fig. 1) was fed with 80% weight hydrogen peroxide as the oxidizer and a blend 30% weight hydrazine (plus liquid catalyst), 57% weight methyl alcohol and water (to lower the combustion temperature).
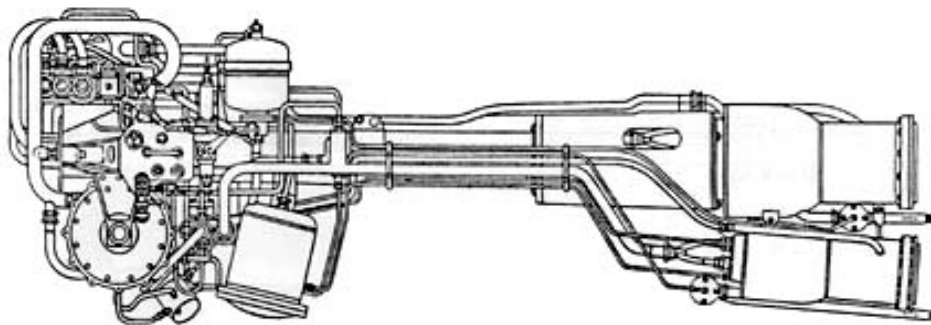
Figure 1. Messerschmidt 163 engine: schematic drawing

Germany made a massive utilization of hydrogen peroxide during World War II: beyond the above applications, it was used for underwater systems (U-Boats) and missiles (V-2). After the war, USA and UK devoted large efforts to develop their own H_2O_2-based propulsive systems: the Reaction Control Systems (RCS) of launchers (i.e. Centuar, Scout) and experimental vehicles (X-1, X-15) were equipped with 90% weight peroxide (for a schematic view of the X-15 see Fig. 2).
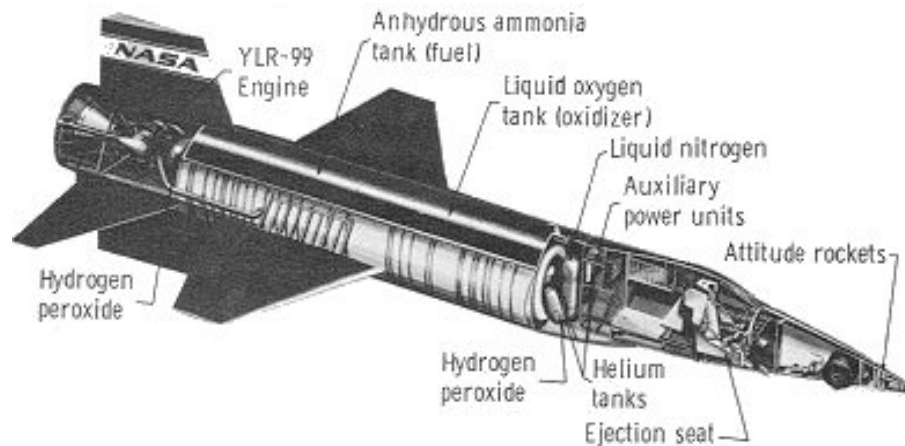
Figure 2. NASA X-15 vehicle: schematic view

The peroxide found its most important propulsive application in the Gamma series rocket engine, which powered the UK Black Knight and Black Arrow vehicles: this engine (shown in Fig. 3) was fed with 85% weight H_2O_2 and kerosene. It successfully powered the Black Knight during 22 sub-orbital flights from the Woomera launch site (Australia) from 1958 to 1965. In 1971, the evolution of the Black Knight (e.g. the Black Arrow) reached the altitude conventionally corresponding to a Low Earth Orbit (LEO), becoming the first (and the last, up to now) launcher fully relying on a H_2O_2-based engine.
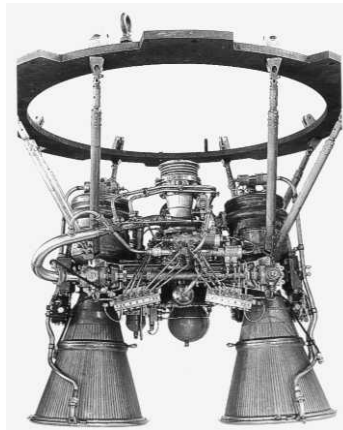
Figure 3. The Gamma-301 engine

After this big success, the peroxide was gradually left, due to the search of propellants able to provide higher propulsive performances, as well as to other considerations not strictly related to technical/scientific issues [3].

Other liquid propellants, both cryogenic (liquid hydrogen/liquid oxygen) and storable (hydrazine/nitrogen tetroxide) currently feed the largest fraction of rocket engines, for both high-thrust level applications (where often solid propellants boosters are used to increase the thrust, as

9

in the Space Shuttle shown in Fig. 4) and low-thrust systems (as the hydrazine-based thruster shown in Fig. 5).

Figure 4. NASA Space Shuttle at lift-off

Figure 5. EADS-ST 400N hydrazine thruster

The only H_2O_2-based system currently in flight service is the RCS of the Russian Soyuz.

But, as stated in the former section, the hydrogen peroxide is coming back, due to the growing importance which the issues related to the reduction of cost and of the environmental impact are assuming during the development, production and maintenance/operation phases of space propulsive systems.

High propulsive performances (at least comparable with the state-of-the-art propellants) are of course *conditio sine qua non* to start the Green Propellants revolution. Table 1 shows a comparison between the specific impulse and the density impulse achievable with hydrazine/nitrogen tetroxide and pure (100% weight) hydrogen peroxide/kerosene (the JP-4 fuel, widely used in aviation applications, has been considered as representative of the kerosene class). Operating conditions typical of bi-propellant rockets used in both RCS and OMS (Orbital Manoeuvring

Systems) have been assumed: pressure levels in the combustion chamber in the range 1-10bar have been considered; the specific impulse is computed for expansion to vacuum. As summarized in Table 1, the specific impulse of the peroxide-based engine is lower (~7%) but the density impulse is higher (~4%), due to the higher density of a stoichiometric mixture of the selected propellants with respect to a stoichiometric mixture of hydrazine/nitrogen tetroxide (see Tab. 2 for the densities of the propellants). Such result can be advantageous in the applications with severe mass/volume constraints (these constraints grow as the dimension of the system decreases, as will be shown later in this section).

The same trends hold for a mono-propellant configuration: the comparison between hydrazine and hydrogen peroxide is summarized in Tab. 3; the peroxide guarantees a lower specific impulse (~17%) but a higher density impulse (~24%).

Table 1. Performances comparison for bi-propellant engines

Propellants	Chemical formula	I_{sp} [s]	ϱI_{sp} [kg/m^3·s]
Hydrazine/nitrogen tetroxide	N_2H_4/N_2O_4	356	447136
JP-4/Hydrogen peroxide	$CH_{1.94}/H_2O_2$	330	466950

Table 2. Density of liquid propellants

Propellants	Density [kg/m^3]
Hydrogen peroxide	1500
JP-4	810
Hydrazine	1450
Nitrogen tetroxide	$CH_{1.94}/H_2O_2$

Table 3. Performances comparison for mono-propellant engines

Propellants	I_{sp} [s]	ϱI_{sp} [kg/m^3·s]
Hydrazine	230	230000
Hydrogen peroxide	191	286500

In both cases, no dramatic decrease of the propulsive performances derives from the replacement of hydrazine with hydrogen peroxide.

Let move now to the storability issue. Hydrogen peroxide has been mostly considered as a very unstable compound, difficult to handle and almost impossible to store for long periods, as required in some propulsive applications. This picture is not completely true, or at least not completely updated: as reported in [4, 5] hydrogen peroxide can be stored for periods longer than 17 years, which means that it is as storable as hydrazine (more information on this point are summarized in Tab. 4).

Table 4. Storability of hydrazine and hydrogen peroxide

Propellant	Storability
Hydrazine	~10 years (sealed)
Hydrogen peroxide (98%)	3+ years (sealed, demonstrated 1965) 15 years (sealed, estimated modern chemistry) 17+ years (vented, demonstrated)

Another factor that strongly affects the choice of a propellant is its toxicity level: when addressing this issue, the advantages related to the utilization of the hydrogen peroxide become more evident. As reported in Tab. 5, the toxicity level for hydrazine is one order of magnitude larger than for hydrogen peroxide (assuming as a toxicity measurement the Personal Exposure Limit of the Occupational Safety and Health Organization, but similar conclusions are attained if different indicators, as the lethal dose or concentration causing the death in 50% of the subjects, are considered): furthermore, hydrazine is a carcinogenic compound. Strong time and cost savings arise from the replacement of a toxic propellant which a much less harmful one.

Table 5. Toxicity of hydrazine and hydrogen peroxide (Ref. [4])

Propellant	Toxicity
Hydrazine	0.1ppm OSHA-PEL 60mg/kg (rat) Oral LD50 570ppm (rat) Inhalation LC50 (4h) Carcinogen Mutagen
Hydrogen peroxide (98%)	1ppm OSHA-PEL 805mg/kg (rat) Oral LD50, 70% H_2O_2 170ppm (rat) Inhalation LC50, 50% H_2O_2

Some other considerations, related to the possible utilization of hydrogen peroxide in non-space systems (for example in gas generators for terrestrial applications) are reported here to underline the benefits of a peroxide-based technology. The products of the H_2O_2 decomposition are oxygen and water vapour, which can be exhausted in the atmosphere with no concern about safety and/or negative effects on the environment. On the other side, the hydrazine decomposition generates hydrogen, which can after-burn in air: the exhaust stream is flammable and odorous too (ammonia is generated along with hydrogen).

Finally, a deeper insight into the miniaturization issues mentioned above is worthwhile in this section. There is an increasing demand for the ability to provide extremely low levels of thrust or impulse bit: the need for micro-propulsion arises in essentially two distinct future mission

scenarios. In the first setting, a more traditional scale type of satellite may be used in a mission which requires its orbital attitude and position to be maintained with unprecedented levels of precision. Extremely small perturbations to the attitude and/or position of the satellite may result because of such effects as solar radiation pressure or gravitational non-uniformities. To offset the perturbations, periodic (or continuous) thrust corrections on the order of micro-Newtons are required. It is important to note that the design challenge here is to develop a propulsion system capable of delivering very low thrust levels: however, the propulsion system itself is not subject to any severe constraints on size, mass or power usage. To this end, electric-based micro-propulsion concepts have been identified as a potential solution.

The second scenario in which micro-scale levels of thrust are required is when the size of the satellite is itself significantly reduced. There is an overall movement toward the development of miniaturized spacecraft which can be used for a number of applications. Having masses in the range of 10÷100kg, these platforms are more commonly known as micro-spacecrafts, according to the classification proposed by the US Air Force Research Laboratory [6] and summarized in Tab. 6.

Table 6. AFRL proposed satellite classification standard

Total Spacecraft Mass [kg]	Description
100-1000	Small spacecraft
10-100	Micro-spacecraft
1-10	Nano-spacecraft
<1	Femto-spacecraft

One of the most promising applications is the use of distributed spacecraft formations to achieve specific mission goals. Distributed spacecraft concept such as formation flying represents a departure from traditional satellite philosophy, which is based on a single, massive multi-functional spacecraft. An excellent example of such a mission is the joint ESA/NASA's laser interferometry space antenna (LISA) program, which is intended to detect gravitational waves in the solar system [7]. In the LISA mission, three satellites having individual masses of 500kg are stationed at a stable Lagrangian point in the solar system (where the gravitational forces from the Earth and the Sun are equal) in a triangular formation separated by 5000000km and must maintain mutual alignments of 30nrad and orbital positions within 10nm. With this level of precision, the perturbation of the radiation pressure from the solar wind is sufficient to upset the operation and must be offset by a thrust level ranging between 1÷100μN with an estimated accuracy of 0.1 μN.

Distributed spacecraft mission architectures offer a number of advantages such as reduced mission cost (production and launch), increased flexibility and reliability and improved data resolution. Owing to the substantially reduced size, the micro-satellites have unique propulsion requirements, including extremely low thrust levels and/or extremely low minimum impulse requirements for orbital manoeuvres and attitude control.

Propulsion systems for these satellites must also satisfy additional mass, volume and power constraints: micro-electromechanical-systems (MEMS) have been identified as potential solutions: several strategies have been identified and are summarized in Tab. 7.

Table 7. A survey of some micro-propulsion initiatives in academia, government and industry in recent years

Thruster type	Specific impulse [s]	Thrust [μN]	Developing agency
H_2O_2-monopropellant	160	1÷1000	NASA GSFC
Cold gas	40÷80	500÷50000	MIT, NASA JPL
Digital solid	200	10÷100000	NASA GRC, TRW, CNES
Vaporizing liquid	75÷125	1÷100	NASA JPL
Ion engine	1400÷2000	0.1÷10	NASA JPL
FEEP	17000	10÷200	University of Pisa

In assessing the relative merit of a given approach, it is important to recognize that each mission specification will have its own set of unique constraints: one micro-propulsion strategy might be an excellent fit for one type of mission but be inappropriate for others. Electrical-based micro-thrusters, e.g. ion engines or FEEP (Field Emission Electrical Propulsion) engines, are capable of delivering very low thrust levels but currently are large in size and mass, and have relatively high power requirements with respect to micro-satellite concepts. Solid propellant devices (e.g. digital micro-thrusters, as the one shown in Fig. 6) are limited primarily by their digital nature: once fired they are not reusable. These devices therefore are constructed in arrays and necessarily have a pre-set number of firings in their lifetime. Another potential problem in micro-satellite applications is that the location of the thrust vector will vary from firing to firing as the devices are depleted: the resulting shift in the thrust location can produce additional perturbations to the attitude of a small satellite, which must be accounted for in each firing.
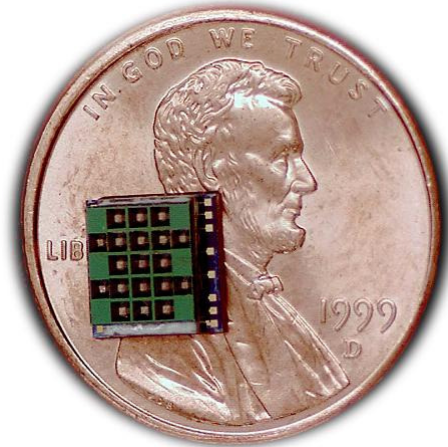
Figure 6. Solid propellant (digital) micro-thruster

Chemical mono-propellants have traditionally be attractive for satellites because they offer relatively high thrust-to-weight ratios owing to the inherently high amount of stored chemical energy per unit mass. This benefit is compounded in MEMS-scale devices because of the interplay of volume and surface area scaling. The mass of propellant is a volumetric quantity which decreases as the cube of the length scale; in contrast, thrust is a surface quantity which depends on the surface area of the nozzle outlet and so decreases as the square of the length scale. Thus, the thrust-to-weight ratio increases linearly with decreases in the device size.

Furthermore, mono-propellant thrusters typically rely upon a catalyzed chemical decomposition of the liquid propellant as the source of energy: as will be shown later in the present work, the efficiency of the catalytic decomposition increases as the surface-to-volume ratio increases. Since the surface-to-volume ratio is inversely proportional to the size of the catalytic chamber, additional benefits should be expected in MEMS devices.

If the higher density impulse of hydrogen peroxide with respect to hydrazine is accounted for in this context, the advantages related to the utilization of H_2O_2 as propellant not only for macro-scale systems but for micro-thrusters too are straightforward.

Despite this huge potential, and the additional benefits of a liquid-fuelled system (e.g. repeatability of the thrust vector, controllability of thrust and impulse bit by regulating the mass flow rate and/or duration) little work in this area has been reported: the 500μN H_2O_2-based micro-thruster developed and successfully fired at the NASA Goddard Space Flight Centre [8] is mentioned here as the most significant R&D effort in this field.

15

1.3 H_2O_2-based propulsive system: fundamentals and design considerations

In the preceding section, hydrogen peroxide has been proved to be a suitable candidate in several propulsive systems and mission scenarios.

Whatever the specific application, the essential operating scheme of a H_2O_2-based engine is illustrated in Fig. 7: the peroxide is fed from a propellant reservoir into an injector which produces a desired pressure drop in the fluid. The injector feeds into a catalytic chamber where the liquid propellant undergoes chemical decomposition and generates gaseous products (oxygen and water vapour) at the chamber outlet. The decomposition process can be described according to the following reaction:

$$H_2O_2 \Rightarrow H_2O + \frac{1}{2}O_2 (\Delta H_R \cong -23000 \frac{cal}{mol})$$
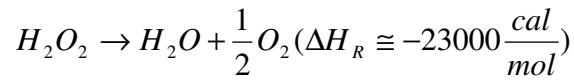
Being highly exothermic, the decomposition produces high temperature gases, which can be expanded through a converging/diverging nozzle (mono-propellant configuration) or enter a combustion chamber to ignite and burn a fuel, both solid or liquid (bi-propellant configuration).

To maximize the heat release in the catalytic chamber, the decomposition should occur in adiabatic conditions.

Please note that a catalytic decomposition has been assumed in the scheme reported in Fig. 7: a thermal decomposition can also occur, but due to the high activation energy the peroxide should be pre-heated to high temperatures (>400°C) to have a reaction proceeding at an appreciable rate [9]. An auxiliary heating device should be necessary, with an increase in power and mass requirements which can be unacceptable, in particular for low-thrust level applications. The main function of the catalyst is to lower the activation energy required to break-up the peroxide molecules [10]: in this way, the decomposition will occur at a sufficient rate in low temperature conditions too.

Moreover, a heterogeneous reaction (promoted by a solid catalyst) is considered: homogeneous (e.g. liquid) catalysts also exist and have been widely investigated and applied on several systems [11]. Anyway, due to the expendable nature of a liquid catalyst (which is ejected from the engine with the products of the reaction) and to the loose of simplicity which would result from having an additional liquid on-board, the homogeneous decomposition has not been investigated in the present work.
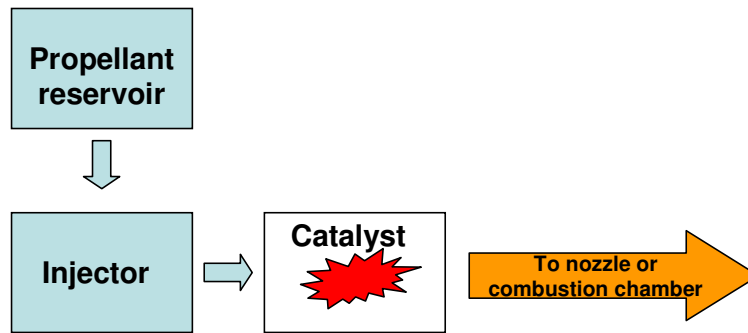
Figure 7. H₂O₂-based engine: operating scheme

The performances of the whole system critically depend on the efficiency of the decomposition process in the catalyst chamber.

Firstly, high conversion rates are required to have high temperatures at the catalyst outlet: hotter gases entering the nozzle (or the combustion chamber) result in turn in a higher specific impulse of the engine.

Typical values of temperatures and specific impulses attainable with a HTP mono-propellant engine are reported in Tab. 8 (where the influence of the initial HTP grade on the performances of the engine is underlined too): complete conversion has been assumed, as well as an adiabatic decomposition process, to evaluate the temperature; the specific impulse is referred to an expansion to vacuum.

Table 8. HTP decomposition temperature and specific impulse

HTP grade (weight percent)	T [K]	Isp [s]
85	907	167
100	1274	191

Another important parameter which is strongly dependent on the catalyst chamber's features is the impulse bit: it is defined as the minimum amount of impulse that can be delivered each time the engine is fired. Assuring a defined impulse bit is particularly important in OMS and RCS, since it represents the limiting resolution of spacecraft control capability from a given thruster at a given location.

The impulse bit magnitude depends upon both the level of thrust and the actuation speed, which in turn depend on the catalyst induction (or response) time, i.e. the time necessary to reach a certain temperature level.

Even in the case of a single firing limited to few milliseconds, the catalyst has to guarantee a long operating life: for example thousands of operations are requested in RCS, hence the need to maintain a high catalytic efficiency over prolonged periods.

Beyond the chemical stability, the catalyst should have good thermo-mechanical properties: severe cyclic loads are expected during the engine firings, in particular for the applications requiring several engine ignitions/shut-offs.

Finally, low mass and low pressure drop catalytic chambers are essential, especially for low scale systems.

Summarizing this chapter, the hydrogen peroxide has been investigated in recent years as an alternative to the most widely employed propellants (hydrazine/nitrogen tetroxide) because of the advantages related to its low toxicity and its low environmental impact. Moreover, the hydrogen peroxide satisfies other technical requirements such as long-term stability and the possibility to start its decomposition without any auxiliary ignition device: this last property is very significant because it allows the engine restart capability without an excessive increase in the overall weight and complexity of the motor structure.

Decomposition rates of practical appliance in propulsive systems can be obtained only by means of suitable catalysts: the catalyst properties and the catalytic reactor design are fundamental aspects for the development of efficient HTP-based engines [12].

The catalyst must exhibit:

- high activity in a wide range of operating conditions (varying from H_2O_2 liquid phase at room temperature to H_2O_2 vapour phase up to the adiabatic decomposition temperature);
- high resistance to thermal and mechanical shocks associated to frequent ignition/shut down cycles;
- high resistance to the stabilizing agents normally added to HTP solutions to improve the long-term storability;
- very short response times;
- small weight and pressure drops.

The development of a catalytic chamber able to simultaneously satisfy the above requirements is not an easy task: different technological solutions have been proposed in literature, but they show some disadvantages, as will be presented in the next chapter: hence the interest in the development of new catalytic systems.

The present work reports the experimental investigations which have been carried out to identify a innovative and efficient configuration, as well as a theoretical/numerical methodology which

has been developed to predict the performances of the catalyst chamber (with particular attention to the conversion rate and the response time), in order to support the development of H_2O_2-based engines and to reduce the time and the cost associated with a trial-and-error approach, upon which such development has widely relied till now.

2. CATALYTIC BED DEVELOPMENT

2.1 Catalytic chambers: traditional solutions and innovative configurations

The heterogeneous catalytic decomposition of hydrogen peroxide has been extensively analyzed in the past and several technological solutions have been proposed, mostly based on the utilization of packed beds (usually composed of metallic screens, as shown in Fig. 8, or ceramic pellets [13]).

Figure 8. Packed bed (metallic screens)

These reactors have some drawbacks, as:

a) high weight and cost: noble metals (i.e. silver, gold, platinum), pure or supported on steel, are considered for the screens; in both cases a heavy and expensive reactor is obtained;

b) large pressure drops;

c) low stability : pure silver screens have a melting point (~1000°C) roughly corresponding to the decomposition temperature of highly concentrated solutions of H_2O_2 (>98% weight), so they can melt or be severely damaged during the engine firings; to overcome this problem, the silver can be deposited on steel screens, but this configuration has a low chemical stability, as the silver layer can be washed out during the operations; metallic screens are also subjected to deactivation, due to the stabilizing agents typically present in HTP solutions

On the other side, ceramic pellets have low thermal/mechanical stability, as they can be crushed (or melted) because of the thermal/mechanical shocks associated with pulsed engine operations.

In the last five years, work has started to investigate a novel configuration which can reduce/eliminate the above problems: the peroxide is injected in a monolithic reactor (as the ones shown in Fig. 9) and flows through parallel channels. Such solution, widely used in chemical

and automotive applications since the Seventies [14], has been recently proposed for aerospace applications too [15, 16, 17] and has been selected as workhorse in the present work.
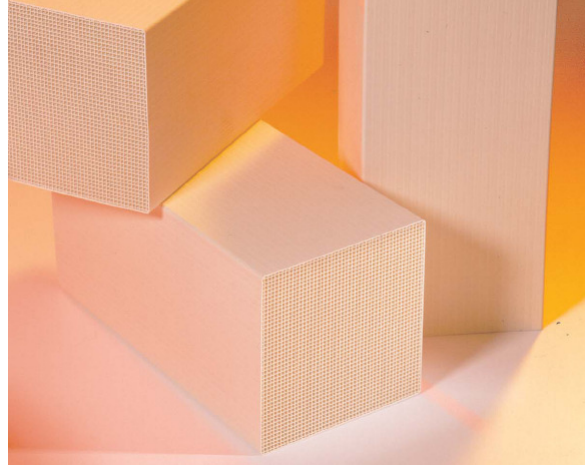
Figure 9. Monolithic supports

A comparison among some properties of packed and monolithic beds is summarized in Tab. 9: assuming similar geometric characteristics and flow conditions, the pressure drop in a monolithic bed is one/two order of magnitude/s smaller than in a packed bed. The solid fraction of monoliths is typically 50% of the value reported for packed beds; the two configurations have similar surface-to-volume ratios.

Table 9. Comparison between packed and monolithic beds (Ref. [18])

	Packed beds	Monolithic beds
Pressure drop, bar/m (Air, 1.1m/s @ 293K)	0.23	$2.8 \cdot 10^{-3}$
Pressure drop, bar/m (Water, $1.3 \cdot 10^{-3}$m/s @293K)	$5.1 \cdot 10^{-3}$	$1.8 \cdot 10^{-4}$
Solid fraction	60	30
Surface-to-volume ratio	2400	1900

A schematic view of the most common monolithic reactor (e.g. the catalytic muffler used to reduce the concentration of NOx, CO and unburned hydrocarbons in the automobile exhausts) is reported in Fig. 10, to help the reader to become familiar with the structure of the reactor.
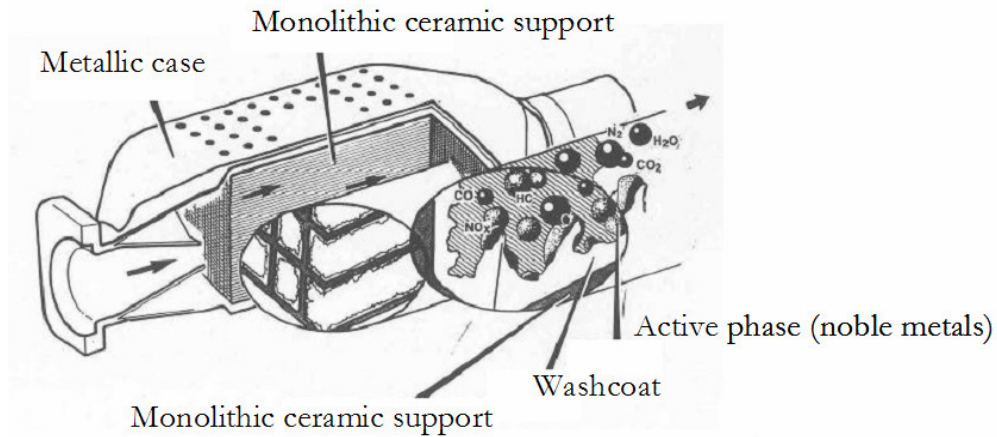
Figure 10. The catalytic muffler: schematic drawing

Three different elements can be identified:

1) the ceramic support: it defines the geometric configuration of the reactor, as well as the main fluid dynamic features of the flow of the reacting mixture; it also determines the global thermal and mechanical properties;

2) the washcoat: the material selected for the support usually has high thermal and mechanical strengths, but it does not provide a sufficiently high surface area; the importance of having an elevated exchange area between the solid and the fluid is straightforward if the basic principle of a heterogeneous reaction is considered: since the reaction occurs at the interface, any increase in the available area will result in a larger number of molecules reacting on it; γ-Al_2O_3 (alumina) is usually selected as the preferred washcoat material, since it has a surface area up to $200 m^2/g$;

3) the active phase: it is responsible for the processes occurring on the interface, e.g. the adsorption of the reagents on the wall, the chemical reaction and the desorption of the products, hence it determines the overall activity of the catalyst, as well as the chemical stability; the active phase can not be used alone (without support/washcoat) since it has not mechanical and thermal properties able to withstand the harsh operating conditions typical of exothermic reactions occurring in adiabatic reactors; moreover, the materials commonly used as active phase do not exhibit high surface areas.

Few data are available in literature on monolithic reactors for space applications, for this reason an experimental investigation has started, aiming at:

- the identification of suitable active phases/supports;
- the characterization of the activity and the stability of the selected catalyst/s.

Recent literature points to manganese-based catalysts as the most promising alternative to metallic catalysts [19]: pure, mixed or supported manganese oxides have been largely investigated. Amongst the oldest known catalysts for H_2O_2 decomposition is the manganese dioxide (MnO_2): it exhibits a high activity, along with Mn_3O_4 and Mn_5O_8, whereas Mn_2O_3 has been found to be completely inactive [20]. The activity of some MnO_x phases (as MnO_2 or Mn_3O_4) has been related to the presence in reaction conditions of different Mn oxidation states and to a high electron mobility.

Generally, mixed oxides have been found to be more active than pure MnO_x systems, due to the presence of metal ions with different charges on the catalyst surface.

H_2O_2 decomposition on Mn oxides supported on different material, as SiO_2, Al_2O_3, SiO_2-Al_2O_3 [19, 21], ZrO_2 [16] and cordierite [15] has been investigated: the results of these studies suggest that the catalytic properties of Mn oxides are markedly influenced by the type of support, hence the interest in new, supported catalyst containing high concentration of surface active species that can be stable under reaction conditions typical of space propulsive applications.

According to these considerations and to the outcome of preliminary tests [12], manganese dioxide has been chosen as the active phase.

Different ceramic supports (titania, zirconia, cordierite) have been investigated: the main features of these materials are listed in Tab. 10.

Both titania and zirconia have a high surface area ($>100m^2/g$) and elevated thermal/chemical stability: in particular, zirconia is able to withstand temperatures as high as 2500K (for this reason it is also considered for the thermal protection systems of hypersonic vehicles).

Cordierite has a much lower surface area (0.5-$2m^2/g$), but it is particularly well suited for applications in systems subjected to thermal cycles, due to the very low thermal expansion ratio which prevents possible damages to the reactor structure as a consequence of the thermally induced stresses: values as low as $10^{-6}/K$ have been reported in the range $300 \div 1275K$, which roughly corresponds to the whole thermal operating envelope of a adiabatic reactor fed with 100% weight hydrogen peroxide (as a comparison, the thermal expansion ratio for stainless steel is about $1.7 \cdot 10^{-5}/K$ at 293K).

Cordierite is widely used in other industrial sectors (i.e. automotive and chemical), hence it is less expensive than other materials and can be easily found in the required shapes and sizes.

Table 10. Ceramic supports investigated in the present work

Name	Composition	Cost	Notes
Titania	TiO_2	-	High surface area, good resistance to acid environment
Zirconia	ZrO_2	Moderate/high	Excellent thermal properties (operating temperature up to 2500K)
Cordierite	$2MgO \cdot 2Al_2O_3 \cdot 5SiO_2$	Moderate	Excellent thermal properties (the lowest thermal expansion ratio)

Ceramic supports have generally a low thermal conductivity, for example values for cordierite are approximately equal to 0.1 W/(m·K), hence a ceramic reactor will operate in conditions very close to the adiabatic regime. On the other side, metals have a much higher thermal conductivity (~15 W/(m·K) for stainless steel), which will result in larger thermal losses and eventually in a decrease of the reactor efficiency, due to a temperature at the reactor exit smaller than the adiabatic value. As will be shown in the next chapters, the thermal conductivity does also affect other important features of the flow inside the catalyst: for this reason a trade-off between ceramic and metallic supports could be worthwhile.

The experimental activities which have been carried out to characterize the novel configurations under investigation in the present work can be classified in two main branches:

a) chemical/physical analysis of the catalyst;

b) measurements of the catalyst's activity/stability.

The first branch aims at the achievement of a qualitative/quantitative characterization of the surface of the catalyst, through the following techniques:

- scanning electron micrographs (SEM);
- X-ray diffraction (XRD);
- Surface area measurements (BET method);
- Temperature programmed reduction (TPR).

The second branch aims at the assessment of the catalyst's performances and at the estimation of the kinetic data which are necessary to design the catalytic reactor.

The following section describes the results of the catalytic activity and stability measurements: the interested reader is referred to the work presented in [22, 23, 24] for more details on the chemical/physical analyses of the catalysts.

2.2 Catalyst's characterization: activity and stability measurements

A semi-batch reactor has been employed to perform the activity and stability measurements: both a picture and a schematic view of the experimental apparatus are shown respectively in Figs. 11-12. Two distinct zones can be identified in the reactor: a lower cylindrical part (with a volume equal to 200cm^3) and a upper flask (volume equal to 2000cm^3) which avoids over-pressures during the decomposition process. The reaction occurs in the lower cylinder, while in the upper flask three openings are available, to allow the catalyst injection, the monitoring of the reactor temperature and the exhaust of the decomposition products.

The reactor is thermo-stated by an electronically-controlled water bath: in order to estimate the kinetics of the reaction, isothermal conditions need to be maintained within the reactor.

A magnetic stirrer guarantees a high degree of uniformity within the reactor (with respect to the dispersion of the catalyst).

The rate of oxygen production is continuously monitored by mass flow meters (two different ranges: 10dm^3/h and 100dm^3/h can be alternatively selected, in order to have a high degree of accuracy on the measured data in a broad range of experimental conditions). This method, unlike other ones (volumetric, titrimetric, refractometric etc.) allows direct measurements of the reaction rate, without any derivative operations.

A trap is inserted at the outlet of the reactor to eliminate some fog that could be carried by the oxygen stream.

Figure 11. Semi-batch reactor: picture
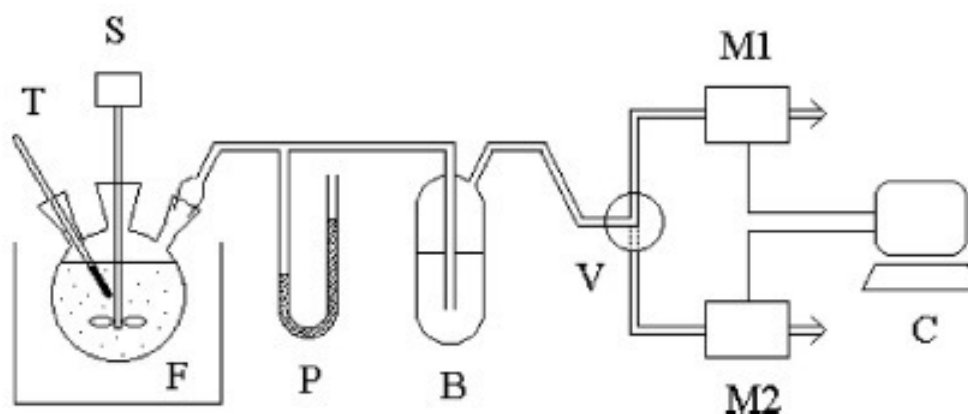
Figure 12. Semi-batch reactor: schematic view (F, flask; T, thermometer, S, stirrer; P, pressure gauge; B, bubbler; V, three-way valve; M1 and M2, flow meters; C, computer)

The first tests have been carried out using pure manganese dioxide and manganese dioxide supported on titania (at different MnO_2 loadings): measurements have been acquired on pure titania to ascertain the possible catalytic activity of the support that is partially uncovered in the catalysts with low manganese contents.

Catalytic tests were also performed on the pure phases MnO_2 and Mn_2O_3. In all the investigated experimental conditions, the support and the Mn_2O_3 phase have shown negligible activity for the hydrogen peroxide decomposition; by contrast, MnO_2 has shown a high activity: these results are coherent with the behaviour observed in literature and summarized above.

Only in one case, Mn_2O_3 has been reported to be more active than MnO_2 [25]: this discrepancy could be due to the different experimental procedure adopted in the cited work, as well as to the influence of test parameters/conditions which have been not properly accounted for, as pointed out by the authors of the above work too.

Two different hydrogen peroxide solutions (50% and 70% weight) have been used; tests at 40°C and 70°C have been carried out.

The catalyst powder which has been used has a grain dimension in the range 71÷150μm.

The results of the experimental characterization of the MnO_2 and MnO_2/TiO_2 catalysts are summarized in Tab. 11.

Table 11. Oxygen flow rate and reaction rate in stationary conditions for MnO_2 and Mn/Ti catalysts

$V_{cat}/V_{sol} \times 10^3$	Temperature °C	H_2O_2 concentration wt%	Oxygen flow rate[a] $dm^3 \cdot h^{-1}$	Reaction rate, $mol \cdot s^{-1} \cdot cm^{-3} \times 10^5$
		MnO_2		
0.15	40	50	0.43	67
0.20	40	50	0.60	70
		2-Mn/Ti		
1	40	50	——	——
1	70	50	0.36	8.3
		5-Mn/Ti		
1	40	50	——	——
1	40	70	0.21	4.9
		7-Mn/Ti		
1	40	50	0.34	8.0
1.5	40	50	0.60	9.3
1	40	70	0.53	12.2
		10-Mn/Ti		
1	40	50	0.43	9.9
1.5	40	50	0.62	9.6
1	40	70	0.66	15.3

[a]Measured at $T = 20°C$ and $P = 1$ bar.

In the above table, the data referred to 7-Mn/Ti and 10-Mn/Ti (the number prefix indicates the concentration of the active phase, as weight percent) show that increasing the hydrogen peroxide concentration from 50% to 70% a nearly proportional increase is obtained, in agreement with a first-order rate equation, as also reported in literature for manganese-based catalysts.

In the experimental conditions of these tests, the amount of decomposed H_2O_2 is small compared to the available reagent, thus the peroxide concentration can be assumed constant during each test and equal to the initial concentration n_0/V_{sol}, where n_0 represents the initial moles of peroxide and V_{sol} the solution volume.

The H_2O_2 decomposition rate per catalyst volume is then given by Eq. (1):

$$-\frac{1}{V_{cat}}\frac{\Delta n}{\Delta t} = k\frac{n_0}{V_{sol}} \tag{1},$$

where V_{cat} represents the catalyst volume and k is the kinetic constant.

By means of Eq. (1), kinetic constants are calculated as mean values from tests performed at the same temperature but with different peroxide concentration and catalyst weights: these values are listed in Tab. 12.

The kinetic constant of MnO_2 is about one order of magnitude higher than those of supported catalysts: however, as discussed earlier, pure manganese dioxide has no interest for practical

appliances. On the other hand, the activity of Mn/Ti catalysts appears notably high: kinetic constant of 7-Mn/Ti and 10-Mn/Ti are comparable to those reported for MnO_2 supported on Al_2O_3 systems [19]. Results from the cited work have been reported in Tab. 13 to allow the direct comparison.

Table 12. Kinetic constant k and molar kinetic constant k' of MnO_2 and Mn/Ti catalysts

Sample	Temperature, °C	k, $s^{-1} \cdot cm^3_{sol} (cm^3_{cat})^{-1} \times 10^3$	k', $s^{-1} \cdot cm^3_{sol} (mol\ MnO_2)^{-1}$
MnO2	40	39	——
2-Mn/Ti	70	4.7	15.7
5-Mn/Ti	40	1.9	3.1
7-Mn/Ti	40	4.8	5.7
10-Mn/Ti	40	5.6	4.3

Table 13. Kinetic constant and molar kinetic constant (Ref. [19])

Base	Catalyst	Impregnated loading, wt%	Calcined loading, wt%	k, $10^{-6}\ s^{-1}$	k', $s^{-1}mol^{-1}$	Relative activity
A305CS/L		1.10	1.18	19.3	0.580	1.5
A305CS/L	RuO_2	0.04	0.01	4.18	15.5	41
A305CS/L	MnO_2	7.27	0.14	19.4	5.67	15
A305CS/L	MnO_2	7.27	0.23	30.4	5.93	16
A305CS/L	Mn_2O_3	7.27	0.33	38.0	4.45	12
A305CS/L	K, Mn_XO_Y	0.15	0.09	10.9	5.17	14
A305CS/L	K, Mn_XO_Y	0.15	0.16	40.6	5.58	15
A305CS/L	PbO	1.50	1.61	8.35	0.376	1
A305CS/L	V_2O_5	0.42	0.40	8.3	0.485	1.3
EAB2	K, Mn_XO_Y	NIA	1.85	133	6.12	16
SAB2	K, Mn_XO_Y	NIA	3.68	146	9.69	26
SABlO	K, Mn_XO_Y	NIA	1.91	54.9	10.8	29
EAB19	K, Mn_XO_Y	N/A	2.61	158	4.07	11
SAB30	K, Mn_XO_Y	N/A	2.64	111	9.87	26

In the examination of the results summarized in Tab. 13, let focus on the data referred to MnO_2 (third and fourth rows) If proper unit conversion is performed, the kinetic constants evaluated in the present work are of the same order of magnitude of the values obtained in [19].

Further analysis of the data reported in Tab. 12 leads to the following observation: increasing the MnO_2 content from 5.3 to 7.3% causes an increase of the molar activity, whereas a further increase to 11% produces a decrease. Thus, there is an optimal MnO_2 content at 7.3%: this could

be explained by taking into account that different manganese species are present on the surface of the catalyst and that their concentration varies with the manganese loading.

Moreover, the decomposition reaction of H_2O_2 on manganese-based catalyst has been suggested to proceed via the following mechanism [20]:

$$H_2O_2 \leftrightarrow HO_2^- + H^+ \tag{2},$$

$$Mn^{4+} + HO_2^- \leftrightarrow Mn^{4+}(HO_2)^- \tag{3},$$

$$Mn^{4+}(HO_2)^- \leftrightarrow Mn^{3+} + HO_2. \tag{4},$$

$$HO_2. + H_2O_2 \leftrightarrow OH \cdot + O_2 + H_2O \tag{5},$$

$$H^+ + OH^- \leftrightarrow H_2O \tag{6}.$$

Hydrogen peroxide solutions are acid [9], hence the step (2) is assumed to be very fast. The adsorption step (3) is also assumed to be fast: the rate determining step is probably the formation of the radical $HO_2 \cdot$. According to this mechanism, the reaction rate depends at the same time on the kinetics of reduction of Mn^{4+} cations and on their concentration. It has been observed that the increase of MnO_2 contents leads to the formation of more Mn^{4+} oxide species and at the same time to a decrease of the mean oxidation state of manganese. The concurrence of such effects can explain the optimal MnO_2 content corresponding to the maximum intrinsic kinetic rate.

Further details on the characterization of the Mn/Ti catalysts can be found in [22].

The second test series has been performed on Mn/Zr systems; a 60% weight hydrogen peroxide solutions has been used; tests at different temperatures (40°C and 70°C) have been performed in this case too; three different types of zirconia (non stabilized, partially stabilized and totally stabilized) have been investigated.

Using the same data reduction procedure followed for the test on Mn/Ti catalysts, the results summarized in Tabs. 14, 15 (respectively at 40°C and 70°C) have been obtained.

Comparing these data with those previously reported in Tab. 12, the higher activity of the Mn/Zr catalysts with respect to the Mn/Ti systems can be inferred.

Further details are reported in [23].

Table 14. Kinetic contant and molar kinetic constant of Mn/Zr catalysts (T=40°C)

Catalyst	$k \cdot 10^3, \dfrac{cm^3_{sol}}{cm^3_{cat}s}$	$k', \dfrac{cm^3_{sol}}{mol_{MnO2}s}$
5-Mn/Zr NS	5.2	9.06
10-Mn/Zr NS	33.9	29.47
5-Mn/Zr PS	n/a	n/a
10-Mn/Zr PS	3.9	3.41
5-Mn/Zr TS	5.5	9.66
10-Mn/Zr TS	17.3	15.07

Table 15. Kinetic contant and molar kinetic constant of Mn/Zr catalysts (T=70°C)

Catalyst	$k \cdot 10^3, \dfrac{cm^3_{sol}}{cm^3_{cat}s}$	$k', \dfrac{cm^3_{sol}}{mol_{MnO2}s}$
5-Mn/Zr NS	10.9	19.02
10-Mn/Zr NS	40.1	34.78
5-Mn/Zr PS	7.1	12.52
10-Mn/Zr PS	9.8	8.52
5-Mn/Zr TS	10.2	17.74
10-Mn/Zr TS	9.3	19.91

The last test series has been performed to characterize the Mn/Cordierite catalysts. A 60% weight hydrogen peroxide solution has been used in these tests; catalysts obtained with different preparation procedure have been compared (more information on the preparation procedure can be found in [24]). The results are summarized in Tab. 16: values comparable to the Mn/Ti system have been obtained.

Table 16. Kinetic contant and molar kinetic constant of Mn/cordierite catalysts (T=40°C)

Catalyst	$k \cdot 10^3, \dfrac{cm^3_{sol}}{cm^3_{cat}s}$	$k', \dfrac{cm^3_{sol}}{mol_{MnO2}s}$
C-IMPRA	1.287	1
C-PRECBC	2.35	1.15
C-PRECAC	3.05	0.99
C-IMPRSV	3.4	2.07

Beyond the activity measurements, a characterization of the stability of the catalysts has been carried out, monitoring the oxygen flow rate as a function of the time. A sample of the data which have been acquired is reported in Fig. 13 for the Mn/Ti catalyst: please note that the behaviour plotted in Fig. 13 is representative of the one observed in all the measurements which have been performed in the present work.

The oxygen flow rates are extremely high at the beginning of the test (for the Mn/cordierite catalyst, peak values as high as $180 dm^3/h$ have been measured) and then decrease with time: this could be due to different effects. The presence of stabilizing components in the hydrogen peroxide solution could cause partial poisoning of the catalyst surface, leading to a decrease of the active sites' concentration. Other hypotheses could be also suggested: under reaction conditions, some MnO_2 reduction could occur, leading to the formation of the Mn_2O_3 phase with consequent loss of activity, according to the considerations previously reported. Moreover, the decrease of the activity could be due to the formation and the subsequent growth of a film of gaseous oxygen in the catalysts' pores that hinders the access of the reactant to the inner surface.
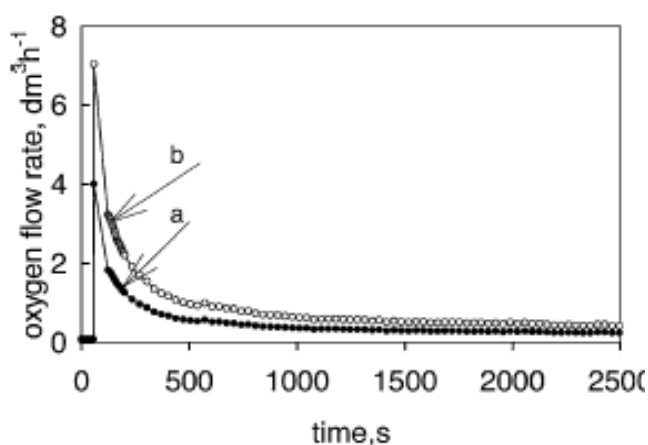
Figure 13. Oxygen flow rate as a function of time for 7-Mn/Ti catalyst, 50% H_2O_2 and T=40°C: a)Vcat/Vsol=10^{-3} and b)Vcat/Vsol=$1.5 \cdot 10^{-3}$

Three main conclusions can be drawn from the results which have been presented in this chapter:

- all the catalysts tested in the present work have shown activities at least comparable to the values reported in literature for similar system, in liquid phase and at room temperatures: this means that a catalytic chamber based on the above catalysts will be able to start the decomposition reaction without any external source of energy; as previously explained, the possibility to achieve an autonomous ignition is a great advantage in space propulsive

systems, as auxiliary devices which increase the mass, the complexity and hence the costs of the structure are not necessary; the importance of this result can be further stressed considering the behaviour of thrusters based on other mono-propellants, as HAN-based (hydroxyl-ammonium-nitrate) blends currently under development, which require catalyst's pre-heating;

- the hydrogen peroxide solutions which have been used in the tests do not correspond to the HTP grade (>85% weight) which is requested for space applications; due to safety issues, commercial grade H_2O_2 (50-70% weight) has been selected; these less concentrated solutions have an amount of stabilizers which is much more elevated than the one corresponding to the HTP grade; despite this drawback, the catalysts have shown a high stability;

- no washcoat has been deposited on the ceramic substrates: a higher resistance to the thermal shocks induced by the ignition/shut off cycles to be expected during the in-flight engine's operations should be expected.

3. MODELLING THE CATALYST FLOW

The heterogeneous decomposition of hydrogen peroxide solutions presents a plenty of physical/chemical processes which should be properly accounted for in any effort aiming at the modelling and the simulation of the flow in the catalytic chamber, as bulk phase phenomena (i.e. the diffusion of reagents/products to/from the catalytic surface), and wall processes (i.e. adsorption, catalytic reaction and desorption).

This complex environment is further complicated by the multi-phase nature of the flow (the propellant enters the reactor in liquid phase, the product of the decomposition reaction exit as gases) and by the coupling of heat and mass transfer.

A full simulation of the real decomposition process should require very complex tools and a huge computational effort. To support the design of the reactor with sufficiently accurate predictions and within reasonable times, the processes which have the greatest influence on reactor's critical parameters (as the reactor volume necessary to achieve a high conversion rate and the response time) need to be identified.

Then simplified tools, able to describe such processes, can be developed.

According to this strategy, a lumped-parameters model of heat and mass transfer in the monolith's channels has been developed and it is described in the following subsection.

3.1 Lumped-parameters approach: the model

In adiabatically occurring exothermic reactions, such as the decomposition of hydrogen peroxide solutions in ceramic monoliths, a multiplicity of steady states can take place [14, 26, 27]. This behaviour rises from a sigmoidal temperature dependence curve for the heat generation rate and a straight line for the heat transfer rate from the catalyst surface to the gas flowing through the channel (see Fig. 14).
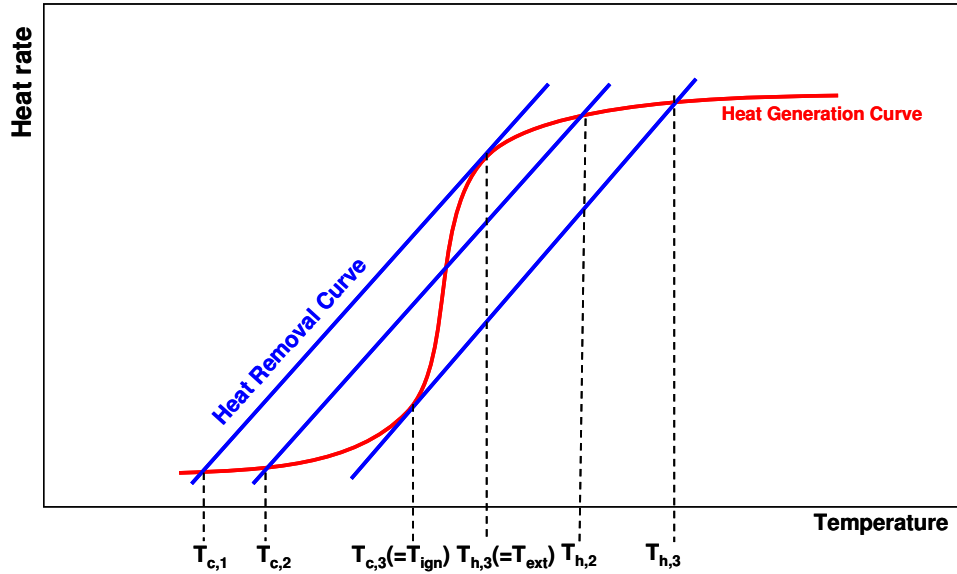
Figure 14. Rate of heat generation and heat transfer vs. catalyst temperature

The intersection points of the two lines define a steady state in which the heat evolved on the catalyst surface is balanced by heat removed from the catalyst surface to the gas. Within a certain range of the catalyst temperature, three intersection points are possible, the middle one being unstable to any perturbation. Upon heating, the catalyst temperature rise corresponds to the lower part of the heat generation curve. After reaching the point of one intersection only, it jumps immediately to the temperature corresponding to the upper part of the heat production curve: this characteristic point is called the ignition or light-off temperature (T_{ign} in Fig. 14). When decreasing the temperature from the high temperature range, similar phenomena will be observed and a sharp temperature drop will occur at the extinction temperature T_{ext}.

Accordingly, the temperature of the monolith will rise slowly with the distance from the inlet until the ignition temperature is reached. In this region the reaction proceeds in the kinetic regime, i.e. the overall process is limited by wall processes. This is usually true for reactants entering the reactor in gas phase: since in space propulsive systems hydrogen peroxide should enter the catalyst chamber as a liquid, the decomposition will proceed in the diffusive regime, that means that the overall process will be limited by bulk processes (diffusion of reagents/products to/from the surface) except for the case of a very low catalyst activity causing the decomposition to be kinetic-limited again.

A typical axial temperature profile along a monolith channel is depicted in Fig. 15. The catalyst surface temperature can exceed the adiabatic decomposition temperature for Lewis number greater than unity: the possibility of this overshoot should be carefully analysed, because it could damage the monolith structure.

34
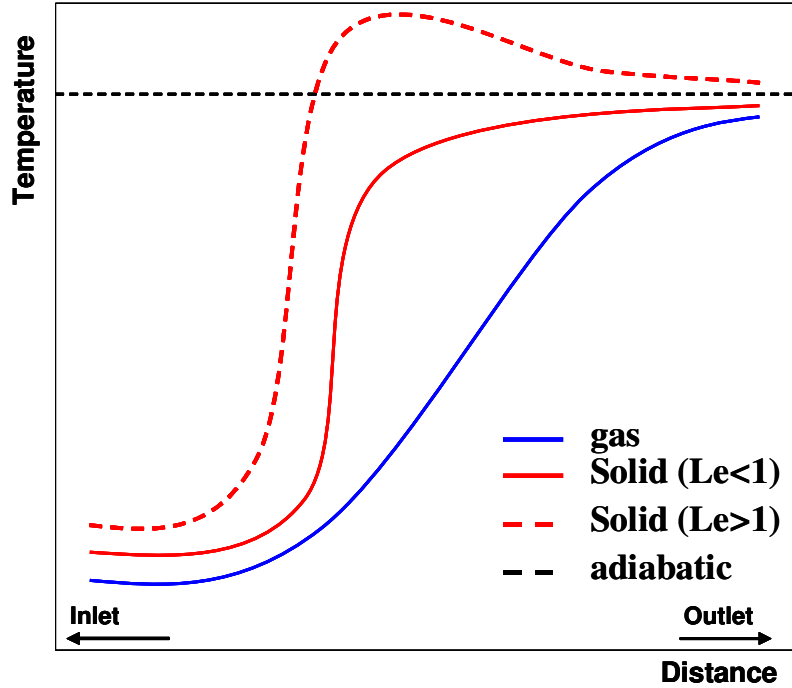
Figure 15. Temperature profiles in the monolith channel

A reliable prediction of the position of the ignition point is *conditio sine qua non* to design an efficient catalyst chamber: a wrong estimation of the ignition abscissa will result in a too short reactor (which will realize a poor conversion) or in a too long monolith (useless volume and mass carried on board).

Simplified models (commonly referred to as lumped-parameters models) have been extensively used to design monolithic reactors in industrial applications, particularly in the automotive and chemical sectors, since the Seventies.

Such models are usually based on the assumptions that the gas-phase temperature, concentration and velocity and the solid-phase temperature are uniform across the monolith cross section: moreover, the axial conduction in the solid and in the gas is not included, and the reaction is assumed to take place only at the monolith surface: the rates of heat and mass transfer are assumed proportional to the difference between the gas and solid temperatures and concentrations [28].

The energy and mass balance for the gas phase are expressed as shown in Eqs. (7), (8):

$$-\rho_g V_m c_{p,g} \frac{\partial T_g}{\partial x} - hS(T_{m,g} - T_w) = \rho_g c_{p,g} \frac{\partial T_{m,g}}{\partial t} \tag{7},$$

$$-V_m \frac{\partial X_{m,g}}{\partial x} - k_d S(X_w - X_{m,g}) = \frac{\partial X_{m,g}}{\partial t} \tag{8}.$$

Heat and mass balances for the solid phase are shown in Eqs. (9), (10):

$$-r\Delta H_R + hS(T_{m,g} - T_w) = \rho_w c_{p,w} \frac{\partial T_w}{\partial t}$$

(9),

$$\frac{\rho_g k_d}{M_g}(X_{m,g} - X_w) = r_S$$

(10).

In Eqs. (7)-(10), t is the time, x the distance along the monolith channel, ρ the mixture density, c_p the mixture constant pressure specific heat, M_g the mixture molecular weight, h and K_d the heat and mass transfer coefficient, V the mixture velocity, T the temperature, S the surface to volume ratio and X the concentration (expressed as mole fraction): the subscripts g and w refer respectively to the gas and the solid (wall) phase. All the gas phase variables are mediated along the monolith cross section: in particular, the gas phase temperature and concentration are defined according to the Eqs. (11), (12) [29].

$$T_{m,g} = \frac{1}{V_m} \int_{A_C} V \cdot T_g \cdot dA_C$$

(11),

$$X_{m,g} = \frac{1}{V_m} \int_{A_C} V \cdot X_g \cdot dA_C$$

(12).

According to the data presented in the previous chapter, the reaction rate r, representing the moles of hydrogen peroxide which are destroyed per unit time and unit area, is assumed proportional to the hydrogen peroxide concentration, as in Eq. (13):

$$r_S = k \cdot C_{H_2O_2}$$

(13).

The kinetic constant k is computed according to the classical Arrhenius formulation (see Eq. (14)):

$$k = A \cdot e^{-\frac{E_a}{RT}}$$

(14).

In Eq. (14), A is the pre-exponential factor, E_a the activation energy and R the universal gas constant.

Eqs. (7)÷(10) constitute an algebraic-differential system which has to be solved to obtain the mean temperature and concentration of the gas phase, as well as the temperature and the concentration at the catalyst surface, as a function of distance and time.

Since variations are assumed to exist along a single spatial direction, the lumped-parameters model is referred to as the one-dimensional (or 1-D) model too in the remainder of this work.

Some additional considerations, aiming at a simplification of the system of Eqs. (7)÷(10), are worthwhile: as the volumetric heat capacity (i.e. the product of the specific heat and the density) is much larger for solids than for gases, the transient behaviour of the reactor will be dominated by the properties of the solid catalyst. In these conditions, the gas-phase temperature and concentration can be assumed to be steady, and the only time-dependent variable is the solid-phase temperature. According to this framework, the unsteady terms in Eqs. (7), (8) can be neglected.

Since the peroxide enter the reactor as a liquid (whose volumetric heat capacity is of the same order of magnitude of the solid, as shown in Tab. 17) the above assumption may lead to errors in predicting the unsteady behaviour (i.e. the response time) of the catalytic chamber: however, as will be shown in the following chapter, only a very limited fraction of the catalytic chamber operates with the liquid phase, hence no strong influence of the above assumptions on the predicted behaviour should be expected.

Table 17. Solid catalyst/liquid H$_2$O$_2$ heat capacities

	Density [kg/m3]	Specific heat [J/kg]
Solid (cordierite)	2600	~1465
Liquid (100% H$_2$O$_2$)	1500	~2500

Let focus now on the terms presented in Eqs. (7)÷(10). The specific heat c_p is assumed constant for the liquid phase, while for the gaseous phase the non-dimensional specific heat is expressed according to the polynomial function shown in Eq. (15), as suggested in [30]:

$$c_p(T)/R = a_1 + a_2T + a_3T^2 + a_4T^3 + a_5T^4 \qquad (15).$$

Two different set of coefficients are considered: the first one is valid in the temperature range 300÷1000K, the second one for temperatures between 1000K and 5000K: the values are reported

in Tabs. 18, 19 for the species of interest in the present work (hydrogen peroxide, water and oxygen).

Table 18. Non-dimensional specific heat coefficients (upper temperature range)

Species	a_1	A_2	a_3	a_4	a_5
H_2O_2	$0.04573167 \cdot 10^2$	$0.0436136 \cdot 10^{-1}$	$-0.14746888 \cdot 10^{-5}$	$0.02348903 \cdot 10^{-8}$	$-0.14316546 \cdot 10^{-13}$
H_2O	$0.02672145 \cdot 10^2$	$0.03056293 \cdot 10^{-1}$	$-0.08730260 \cdot 10^{-5}$	$0.12009964 \cdot 10^{-9}$	$-0.06391618 \cdot 10^{-13}$
O_2	$0.03697578 \cdot 10^2$	$0.06135197 \cdot 10^{-2}$	$-0.12588420 \cdot 10^{-6}$	$0.01775281 \cdot 10^{-9}$	$-0.11364354 \cdot 10^{-14}$

Table 19. Non-dimensional specific heat coefficients (lower temperature range)

Species	a_1	a_2	a_3	a_4	a_5
H_2O_2	$0.03388753 \cdot 10^2$	$0.06569226 \cdot 10^{-1}$	$-0.14850125 \cdot 10^{-6}$	$-0.04625805 \cdot 10^{-7}$	$0.02471514 \cdot 10^{-10}$
H_2O	$0.03386842 \cdot 10^2$	$0.033474982 \cdot 10^{-1}$	$-0.06354696 \cdot 10^{-4}$	$0.06968581 \cdot 10^{-7}$	$-0.02506588 \cdot 10^{-10}$
O_2	$0.03212936 \cdot 10^2$	$0.11274864 \cdot 10^{-2}$	$-0.05756150 \cdot 10^{-5}$	$0.13138773 \cdot 10^{-8}$	$-0.08768554 \cdot 10^{-11}$

For the gas phase, the specific heat of the mixture is computed as shown in Eq. (16):

$$c_p = \sum_{i=1}^{Nsp} X_i c_{p,i} \tag{16},$$

while the mixture density is computed according to the ideal gas equation of state (Eq. (17)):

$$\rho = \frac{P}{R_{mix} T} \tag{17},$$

where the specific gas constant R_{mix} is computed as shown in Eq. (18):

$$R_{mix} = \frac{R}{\sum_{i=1}^{Nsp} X_i M_i} \tag{18}.$$

In Eq. (17), the pressure is assumed to be constant: as the monolithic beds are characterized by low pressure drops (with respect to packed beds, as underlined in the previous chapter) this

assumption should not bring errors in the prediction of the reactor performances. This statement will be verified in the following chapter.

The transport coefficients (viscosity, thermal conductivity, diffusion coefficient) do not appear directly in Eqs. (7)÷(10), but their values are used to compute the heat and mass transfer coefficients by means of the Nusselt and Sherwood numbers which will be defined later in this section.

For the liquid phase, Eq. (19) is used to compute the viscosity [31]:

$$\ln \mu = A + \frac{B}{T} + C \cdot T + D \cdot T^2 \tag{19}$$

In Eq. (19), the temperature is expressed in K, the viscosity in cP; the constant A, B, C, D have been computed from experimental data and are reported in Tab. 20 for hydrogen peroxide and water .

Table 20. Constants in Eq. (19): evaluation of liquid-phase viscosity

Species	A	B	C	D
H_2O_2	-3.179	$1.160 \cdot 10^3$	$8.06 \cdot 10^{-4}$	$-2.689 \cdot 10^{-6}$
H_2O	-24.71	$4.209 \cdot 10^3$	$4.527 \cdot 10^{-2}$	$-3.376 \cdot 10^{-5}$

The thermal conductivity is computed from Eq. (20), which has been also obtained as a polynomial fit of experimental data [31]:

$$\lambda = A + B \cdot T + C \cdot T^2 \tag{20}$$

In Eq. (20), the temperature is expressed in K and the thermal conductivity in W/(m·K): the constants A, B, C are reported in Tab. 21.

Table 21. Constants in Eq. (20): evaluation of liquid-phase thermal conductivity

Species	A	B	C
H_2O_2	$-1.954 \cdot 10^{-1}$	$3.374 \cdot 10^{-3}$	$-3.667 \cdot 10^{-6}$
H_2O	$3.838 \cdot 10^{-1}$	$5.254 \cdot 10^{-3}$	$-6.369 \cdot 10^{-6}$

Finally, the binary diffusion coefficient of hydrogen peroxide in water has been computed according to Eq. (21), as suggested in [26]:

$$D_{i,j} = D_{i,j}^{ref} \frac{\mu_{ref}}{\mu} \frac{T}{T_{ref}}$$ (21).

The suffix *ref* means that the variables are computed at a reference temperature (T_{ref}=293K). The viscosity and thermal conductivity of a liquid mixture of hydrogen peroxide and water are computed according to Eqs. (22), (23):

$$\mu_{mix} = Y_{H2O2} \cdot \mu_{H2O2} + Y_{H2O} \cdot \mu_{H2O}$$ (22),

$$\lambda_{mix} = Y_{H2O2} \cdot \lambda_{H2O2} + Y_{H2O} \cdot \lambda_{H2O}$$ (23),

where Y_{H2O2} and Y_{H2O} are the mass fractions of respectively hydrogen peroxide and water.

Please note that the liquid solution of hydrogen peroxide is treated as a single species everywhere in the model but in the computation of the transport coefficients: for this reason no formulas similar to Eqs. (22), (23) have been reported for the liquid mixture density and specific heat.

The following additional considerations on the evaluation of the liquid-phase transport coefficients are worthwhile: diffusion in liquids occurs at a rate much slower than in gases, due to the much smaller diffusion coefficients (roughly equal to $10^{-5} m^2/s$ for gases and to $10^{-9} m^2/s$ for liquids). For this reason, reactions occurring in liquid phase are mostly diffusion-limited, as stated at the beginning of this chapter.

According to this framework, a high activity of the catalyst could be not sufficient to assure a successful start of the decomposition process of the hydrogen peroxide flowing through the catalytic chamber, that means that despite a fast reaction at the solid/liquid interface, the process would not proceed further, due to a very slow diffusion of the products/reagents from/to the wall.

Fortunately, experimental observations and theoretical models suggest that the diffusion process during the liquid-phase decomposition of hydrogen peroxide can proceed at a rate much faster than the value estimated using the molecular transport coefficients.

As observed in [32], phenomena similar to nucleate boiling occur during the decomposition of H_2O_2 solutions on silver wires: at concentrations lower than 60% weight, a regular evolution of oxygen bubbles over the entire surface has been reported, but at higher concentrations the gas surrounds the catalyst on all sides and the appearance is much like that of a surface from which

film boiling is occurring. This change is similar to the transition from nucleate to film boiling commonly observed in heat transfer, with the important difference that an inert gas is also being generated simultaneously.

The nucleate boiling promotes the exchange of heat and mass to/from the wall: a strong increase (up to one order magnitude and more) in the heat and mass transfer coefficients should be expected in these conditions, as confirmed by the data reported in Fig. 17 [33].
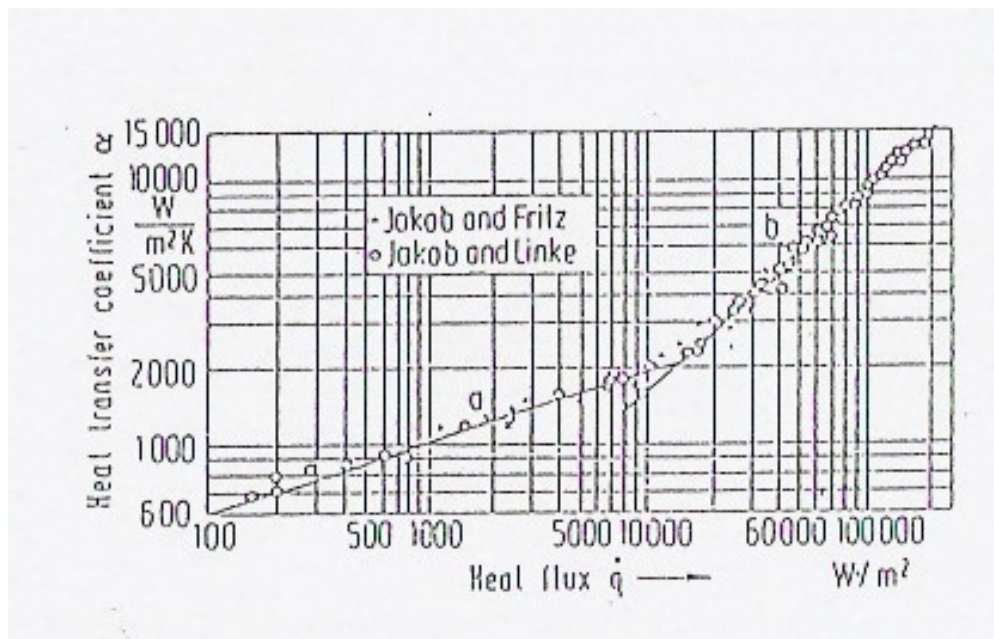
Figure 16. Heat transfer in boiling water at 100°C on a horizontal heated surface; curve a: stagnant boiling region, curve b: nucleate boiling region

A more detailed analysis of the above phenomena, including both a physical explanation of the origin of bubbles evolution during the hydrogen peroxide decomposition and a quantitative estimation of the impact on heat and mass transfer, has been reported in [34]. As the catalyst surface presents a porous structure, bubbles can form inside the pores during a liquid-phase reaction with gas production; this effect also occurs in liquid-phase exothermic reactions. Since the decomposition of liquid hydrogen peroxide involves both heat release and oxygen production, an amplification of these effects should be expected.

The bubbles can leave the pores, generating a strong disturbance and intensifying the outer heat and mass transfer: in this case the appearance of bubbles on the surface is observed. Summarizing the procedure reported in [34], the bubbles will appear if the following condition is verified:

$$\frac{d_{pore}^2 \cdot C \cdot \upsilon \cdot R \cdot T}{\sigma} > \sqrt{\frac{4 \cdot D_{O2} \cdot \sigma \cdot H}{3 d_{pore} \cdot r_v \cdot \upsilon \cdot R \cdot T}} \tag{24}$$

In (24), d_{pore} is the mean diameter of the pore on the catalyst surface, C is the concentration of hydrogen peroxide, υ the stoichiometric coefficient of the gas evolved during the reaction (0.5 for oxygen during H_2O_2 decomposition), σ is the surface tension of the hydrogen peroxide, D_{O2} the diffusion coefficient of O_2 in liquid H_2O_2, H the Henry constant, and r_v the volumetric reaction. Hereinafter, following the nomenclature presented in [34], let denote the left hand side in (24) $y_{displace}$, and the right hand side y_{cr}.

Substituting the proper values, condition (24) has been verified to hold in the operating conditions of interest in the present work: please note that the diffusion coefficient of oxygen in hydrogen peroxide, the surface tension, the Henry constant and the activation energy reported in [34] have been used in the present calculations and are summarized in Tab. 22; typical values of mean pore diameters for cordierite monoliths (as suggested in [14]) have been used; different values of the pre-exponential factor A have been considered to account for different catalyst's activity; the effect of different HTP grade has been investigated too. The results are summarized in Tabs 23-26.

Table 22. Parameters in Eq. (24)

D_{O2} [m^2/s]	$2.41 \cdot 10^{-9}$
H [-]	$2.92 \cdot 10^{-2}$
σ [N/m]	$72.8 \cdot 10^{-3}$
E_a [J/mol]	44100

Table 23. Verification of bubbles appearance (HTP 85% weight, high catalyst activity)

A [1/s]	d_{pore} [m]	HTP grade	T [K]	$y_{displace}$ [m]	y_{cr} [m]
$2.1 \cdot 10^6$	3-21	85	300	$7.13 \cdot 10^{-3}$-$3.50 \cdot 10^{-1}$	$2.99 \cdot 10^{-7}$-$1.13 \cdot 10^{-7}$

Table 24. Verification of bubbles appearance (HTP 85% weight, low catalyst activity)

A [1/s]	d_{pore} [m]	HTP grade	T [K]	$y_{displace}$ [m]	y_{cr} [m]
$2.1 \cdot 10^3$	3-21	85	300	$7.13 \cdot 10^{-3}$-$3.50 \cdot 10^{-1}$	$9.47 \cdot 10^{-6}$-$3.58 \cdot 10^{-6}$

Table 25. Verification of bubbles appearance (HTP 100% weight, high catalyst activity)

A [1/s]	d_{pore} [m]	HTP grade	T [K]	$y_{displace}$ [m]	y_{cr} [m]
$2.1 \cdot 10^6$	3-21	100	300	$6.80 \cdot 10^{-3}$-$3.33 \cdot 10^{-1}$	$3.07 \cdot 10^{-7}$-$1.16 \cdot 10^{-7}$

Table 26. Verification of bubbles appearance (HTP 100% weight, low catalyst activity)

A [1/s]	d_{pore} [m]	HTP grade	T [K]	$y_{displace}$ [m]	y_{cr} [m]
$2.1 \cdot 10^3$	3-21	100	300	$6.80 \cdot 10^{-3}$-$3.33 \cdot 10^{-1}$	$9.70 \cdot 10^{-6}$-$3.67 \cdot 10^{-6}$

A similar approach can be followed to evaluate the heat and mass transfer intensification in exothermic reactions: in this case, vapour will be generated inside the pore, but the overall effect is similar to the one reported above for reactions with gas production. In these conditions, the diffusion coefficient can be evaluated according to Eq. (25) [35]:

$$D_{eff} = \frac{\lambda_{liq}}{\rho_{liq} \cdot c_p} \tag{25}$$

which gives a value several times greater than a molecular diffusion coefficient.

This conclusion is of straightforward importance for an effective utilization of liquid hydrogen peroxide in space propulsive applications.

Let consider now the evaluation of the transport coefficients for the gas phase: following the classical kinetic theory, the viscosity is computed according to Eq. (26) [31]:

$$\mu = 26.69 \frac{(M \cdot T)^{\frac{1}{2}}}{\sigma_s^2 \cdot \Omega_v} \tag{26}$$

where the viscosity is expressed in μP, M is the molecular weight in g/mol, σ_s is the hard sphere diameter in Angstrom and Ω_v is the viscosity collision integral (dimensionless, equal to unity if the molecules do not attract each other).

The viscosity collision integral is computed according to Eq. (27), proposed by Neufield et al. [31] and convenient for computer applications:

$$\Omega_v = A \cdot (T^*)^{-B} + C \cdot e^{-D \cdot T^*} + E \cdot e^{-F \cdot T^*} \tag{27}$$

The constants *A-F* are reported in Tab. 27, while the dimensionless temperature *T** is related to the temperature and the characteristic energy ε through Eq. (28):

$$T^* = \frac{k_B}{\varepsilon} T \tag{28},$$

where k_B is the Boltzmann constant. The values of ε/k_B and σ_s for hydrogen peroxide, water vapour and oxygen are reported in Tab. 28. [36]. Eq. (27) is applicable for $0.03 < T^* < 100$ with an average deviation of only 0.064%.

Table 27. Constants in Eq. (27): evaluation of viscosity collision integrals

A	*B*	*C*	*D*	*E*	*F*
1.16145	0.14874	0.52487	0.77320	2.16178	2.43787

Table 28. Constants in Eq. (28): evaluation of the dimensionless temperature *T**

Species	ε/k_B [T]	σ_s [Angstrom]
H_2O_2	107.400	4.73
H_2O	572.400	2.605
O_2	107.400	3.621

The gas phase conductivity is computed as shown in Eq. (29) [31]:

$$\frac{\lambda \cdot M}{\mu \cdot c_v} = 1 + \frac{9}{4} \cdot \frac{1}{c_p/R - 1} \tag{29},$$

where *M* is the molecular weight in kg/mol and c_v the constant volume specific heat: Eq. (29) si the well known Eucken correlation for polyatomic gases.

The binary diffusion coefficients are computed according to Eq. (30) [31]:

$$D_{AB} = 0.00266 \frac{T^{\frac{3}{2}}}{P \cdot M_{AB} \cdot \sigma_{AB} \cdot \Omega_D} \tag{30},$$

where D_{AB} is expressed in cm^2/s, P is the pressure in bar, M_{AB} (g/mol) and σ_{AB} (Angstrom) are evaluated according to Eqs. (31), (32) and Ω_D is the diffusion collision integral (dimensionless).

$$M_{AB} = \frac{2}{\frac{1}{M_A} + \frac{1}{M_B}}$$

(31),

$$\sigma_{AB} = \frac{1}{2}(\sigma_A + \sigma_B)$$

(32).

Neufield proposed the formula shown in Eq. (33) to evaluate the diffusion collision integral:

$$\Omega_D = \frac{A}{(T^*)^B} + \frac{C}{e^{DT^*}} + \frac{E}{e^{FT^*}} + \frac{G}{HT^*}$$

(33);

constants A-H are reported in Tab. 29; the dimensionless temperature T^* is defined according to Eq. (34):

$$T^* = \frac{kT}{\varepsilon_{AB}}$$

(34),

where ε_{AB} is computed as shown in Eq. (35):

$$\varepsilon_{AB} = (\varepsilon_A \cdot \varepsilon_B)^{\frac{1}{2}}$$

(35).

Table 29. Constant in Eq. (34): evaluation of diffusion collision integrals

A	B	C	D	E	F	G	H
1.06036	0.15610	0.19300	0.47635	1.03587	1.52996	1.76474	3.89411

Finally, the viscosity of the gaseous mixture is computed from the values of the single components using the semi-empirical formula due to Wilke and modified by Bird [36], shown in Eqs. (36):

$$\mu_{mix} = \sum_{k=1}^{Nsp} \frac{X_k \cdot \mu_k}{\sum_{j=k}^{Nsp} X_j \cdot \Phi_{kj}} \tag{36},$$

where:

$$\Phi_{k,j} = \frac{1}{\sqrt{8}} \left(1 + \frac{M_k}{M_j}\right)^{-\frac{1}{2}} \left(1 + \left(\frac{\mu_k}{\mu_j}\right)^{\frac{1}{2}} \left(\frac{M_j}{M_k}\right)^{\frac{1}{4}}\right)^2 \tag{37},$$

while the thermal conductivity the combination averaging formula reported in Eq. (38) is used [36]:

$$\lambda_{mix} = \frac{1}{2} \left(\sum_{k=1}^{Nsp} X_k \lambda_k + \frac{1}{\sum_{k=1}^{K} X_k / \lambda_k} \right) \tag{38}.$$

The coefficient diffusion in a multi-component mixture is computed according to Eq. (39) [36]:

$$D_{k,mix} = \frac{1 - Y_k}{\sum_{j \neq k}^{Nsp} X_j / D_{j,k}} \tag{39}.$$

Once the transport properties have been computed, the heat and mass transfer coefficients which appear in Eqs. (7)-(10) can be evaluated, using the Nusselt and Sherwood numbers, defined according to Eqs. (40), (41):

$$Nu = \frac{h \cdot d_h}{\lambda_{mix}} \tag{40},$$

$$Sh = \frac{k_d \cdot d_h}{D_{mix}} \tag{41},$$

where d_h is the hydraulic diameter of the monolith channels, defined as shown in Eq. (42):

$$d_h = \frac{4A_c}{p} \tag{42}.$$

In Eq. (42), A is the cross sectional area of the channel and p the perimeter (in this way, the hydraulic diameter is equal to the diameter for the case of circular and square section).

Due to the analogy between the transport equations of energy and species, the Sherwood number is assumed to be equal to the Nusselt number. Let demonstrate such assumption for a hydro-dynamically fully developed flow in an axis-symmetrical channel, with no heat (or mass) generation: in this case, the balance of energy and of species i on an elementary volume can be written as shown in Eqs. (43), (44):

$$\frac{u}{\alpha}\frac{\partial T}{\partial x} = \frac{1}{r}\frac{\partial}{\partial r}\left(r\frac{\partial T}{\partial r}\right) + \frac{\partial^2 T}{\partial x^2} \tag{43},$$

$$\frac{u}{D}\frac{\partial X_i}{\partial x} = \frac{1}{r}\frac{\partial}{\partial r}\left(r\frac{\partial X_i}{\partial r}\right) + \frac{\partial^2 X_i}{\partial x^2} \tag{44};$$

where x and r are respectively the axial and radial coordinate, u is the axial velocity, D is the diffusion coefficient of species i in a multi-component mixture and α is the thermal diffusivity, defined according to Eq. (45):

$$\alpha = \frac{\lambda}{\rho \cdot c_p} \tag{45}.$$

Eqs. (43) and (44) are formally similar (and identical if the thermal diffusivity is equal to the mass diffusivity), hence their solution will be similar. Further information can be inferred writing these equations in non-dimensional form, as shown in Eqs. (46), (47):

$$\frac{\partial^2 \theta}{\partial r^+} + \frac{1}{r^+}\frac{\partial \theta}{\partial r^+} = \frac{u^+}{2}\frac{\partial \theta}{\partial x^+} - \frac{1}{(\mathrm{Re}\cdot \mathrm{Pr})^2}\frac{\partial^2 \theta}{\partial x^{+2}} \tag{46},$$

$$\frac{\partial^2 X_i}{\partial r^+} + \frac{1}{r^+}\frac{\partial X_i}{\partial r^+} = \frac{u^+}{2}\frac{\partial X_i}{\partial x^+} - \frac{1}{(\mathrm{Re}\cdot Sc)^2}\frac{\partial^2 X_i}{\partial x^{+2}} \tag{47},$$

where the non-dimensional variables x^+, r^+, u^+ and θ are defined according to Eqs. (48)÷(51):

$$x^+ = \frac{x/r_0}{\mathrm{Re}\,\mathrm{Pr}} \qquad (48),$$

$$r^+ = \frac{r}{r_0} \qquad (49),$$

$$u^+ = \frac{u}{V} \qquad (50),$$

$$\theta = \frac{T_w - T}{T_w - T_{in}} \qquad (51).$$

x^+ is commonly referred to as the Graetz number; the Reynolds and Prandtl number are defined according to Eqs. (52), (53):

$$\mathrm{Re} = \frac{\rho V d_h}{\mu} \qquad (52),$$

$$\mathrm{Pr} = \frac{\nu}{\alpha} \qquad (53),$$

where ν is the kinematic viscosity.

As demonstrated in [29], the Nusselt and Sherwwod numbers can be directly obtained as solutions of the Eqs. (46) and (47):

$$Nu = F(x^+, r^+, \mathrm{Re}, \mathrm{Pr}) \qquad (54),$$

$$Sh = G(x^+, r^+, \mathrm{Re}, Sc) \qquad (55);$$

functions F and G in Eqs. (54), (55) will have the same expression, due to the formal analogy between Eqs. (46) and (47): moreover, if the Prandtl and the Schmidt numbers are equal, the Nusselt and the Sherwood number will be equal too. As the Schmidt number can be defined according to Eq. (56):

$$Sc = \frac{\nu}{D} = \frac{\nu}{\alpha} \cdot \frac{\alpha}{D} = \mathrm{Pr} \cdot Le \qquad (56),$$

this condition is verified if the Lewis number is equal to unity (which is equivalent to say that the thermal diffusivity is equal to the mass diffusivity, as stated formerly in this section). As will be shown in the next paragraph, the Lewis number is close to unity for the gaseous mixture of interest in the present work.

The above considerations, derived for a circular section, can be extended to other geometries too. Eqs. (54) and (55) can be simplified assuming a thermally fully developed flow: recalling the Reynolds analogy, this condition is true for most gases, which have a Prandtl number of O(1) (liquid metals usually have Pr<<1, while a Prandtl number much greater than unity is typical of oils): constant values, depending only on the geometry of the channel cross section, as well as on the thermal boundary condition at the wall, are obtained in this case.

Some examples are reported in Tab. 30, where a laminar flow is assumed and two different boundary conditions (constant heat rate and constant temperature), are considered [29].

Table 30. Nusselt number for fully developed flows in tubes of various cross section

Cross section shape	b/a	Nu_Q	Nu_T
○	-	4.364	3.66
□	1.0	3.63	2.98
▭	2.0	4.11	3.39
▭	3.0	4.77	
▭	4.0	5.35	4.44
══	∞	8.235	7.54
△	-	3.00	2.35

For turbulent flows, no constant values of the Nusselt and Sherwood numbers can be computed, also in the case of a hydro-dynamically/thermally fully developed flow: dependences on the Reynolds and Prandtl number need to be accounted for, as summarized in Tab. 31 [29].

As can be inferred from the examination of the data reported in Tab. 31, a large increase of the Nusselt number should be expected in turbulent flow, due to the macroscopic effect of the turbulence, which greatly enhances the heat (and the mass) transfer rates between the fluid and the wall with respect to the laminar case, where heat and mass exchange does only occur on microscopic scale.

Table 31. Nusselt numbers for fully developed turbulent flow in a circular tube with constant heat rate

Re \\ Pr	laminar	10^4	10^5	10^6
0.0	4.364	6.30	6.84	7.06
0.001	-	6.30	6.84	8.12
0.003	-	6.30	7.10	12.8
0.01	-	6.43	8.90	30.5
0.03	-	6.90	15.9	80.5
0.5	-	26.3	142	895
0.7	-	31.7	178	1150
1.0	-	37.8	222	1470
3.0	-	61.5	404	2900
10	-	99.8	690	5220
100	-	205	1510	12000
1000	-	380	2830	22600

The following consideration is worthwhile to conclude this section: besides the regions of the reactor where the mixture is completely in liquid phase or fully gaseous, a zone exists where both liquid and gas are present. In this zone, proper modelling of the flow (hence the correct evaluation of any variable, including density, specific heat and transport coefficients) is not available: for this reason, bridging formulas, able to guarantee continuity between the liquid-phase properties and the gas-phase properties, have been used. No references have been identified in literature to assess the accuracy of these formulas.

3.2 Lumped-parameters approach: the solution procedure

In order to solve the algebraic-differential system of Eqs. (7)÷(10), which are reported here again for the sake of the reader:

$$-\rho_g V_m c_{p,g} \frac{\partial T_g}{\partial x} - hS(T_{m,g} - T_w) = 0 \tag{7}$$

$$-V_m \frac{\partial X_{m,g}}{\partial x} - k_d S(X_w - X_{m,g}) = 0 \tag{8}$$

$$-r\Delta H_R + hS(T_{m,g} - T_w) = \rho_w c_{p,w} \frac{\partial T_w}{\partial t} \tag{9},$$

$$\frac{\rho_g k_d}{M_g}(X_{m,g} - X_w) = r_S \tag{10},$$

proper boundary conditions need to be specified at the reactor inlet and at the initial time. The partial derivatives are then replaced with finite differences, in order to allow the numerical solution of the system. If only steady-state conditions are of interest, the time derivative in Eq. (9) can be neglected, and the system can be written in non-dimensional form as shown in Eqs. (7')÷(10'):

$$\frac{\partial T_g}{\partial x^+} = Nu(T_{m,g} - T_w) \tag{7'},$$

$$\frac{\partial X_{m,g}}{\partial x^+} = \frac{Sh}{Le}(X_w - X_{m,g}) \tag{8'},$$

$$r\Delta H_R - h(T_{m,g} - T_w) = 0 \tag{9'},$$

$$\frac{\rho_g k_d}{M_g}(X_{m,g} - X_w) = r_S \tag{10'}$$

The differential Eq. (9) turns into the algebraic Eq. (9'): due to the expression of the reaction rate, such equation is non-linear, hence a proper iterative procedure is necessary to find its root/s.

Eq. (9) represents the balance between the heat generated by the chemical reaction at the wall and the heat removed from the wall: multiple solutions can exist (please recall Fig. 14 at the beginning of this chapter) and this behaviour adds complexity to the solving procedure. Most methods only work if the non-linear equation exhibits a monotonic behaviour [37] and this is not the case of Eq. (9) which allows the existence of multiple zeros. For this reason, the solving procedure has been split in two stages: firstly, the temperature range where the actual value/s is/are expected is divided in one to three sub-ranges, where Eq. (9) exhibits a monotonic behaviour; then, the bisection method (selected for its robustness) is applied in each of the above sub-ranges to find the roots. If three solutions are obtained, the middle one is discarded (as it is unstable): for the case of cold-starts, the minimum temperature value is selected, while for the case of hot-starts the highest temperature value is chosen (according to the considerations expressed at the beginning of this chapter).

3.3 Distributed-parameters approach: the model

Commercial Computational Fluid Dynamics (CFD) codes currently available on the market are able to solve the full set of differential equations describing the viscous flow of a mixture of chemically reacting gases.

The Fluent 6.0 solver allows a careful treatment of chemical species diffusion in the species transport and energy equations: such treatment is important when details of the molecular transport processes are significant (i.e. in diffusion-dominated laminar flows, as the decomposition of hydrogen peroxide in monolithic reactors).

For multi-component systems it is not possible, in general, to derive relations for the diffusion fluxes containing the gradient of only one component (i.e. the classical Fick law). Here, the Maxwell-Stefan equations will be used to obtain the diffusive mass flux: this will lead to the definition of generalized Fick's law diffusion coefficients [38]. This method is preferred over computing the multi-component diffusion coefficients since their evaluation requires the computation of N^2 co-factor determinants of size (N-1)x(N-1), and one determinant of size NxN [39], where N is the number of chemical species.

The Maxwell-Stefan equations can be written as shown in Eq. (57) [40]:

$$\sum_{j=1,j\neq i}^{N} \frac{X_i X_j}{D_{ij}} \left(V_j - V_i\right) = d_i - \frac{\nabla T}{T} \sum_{j=1,j\neq i}^{N} \frac{X_i X_j}{D_{ij}} \left(\frac{D_{T,j}}{\rho_j} - \frac{D_{T,i}}{\rho_i}\right) \tag{57},$$

where V is the diffusion velocity, $D_{i,j}$ the binary mass diffusion coefficient and D_T the thermal diffusion coefficient.

For an ideal gas the Maxwell diffusion coefficients are equal to the binary diffusion coefficients. If the external force is assumed to be the same on all species and the pressure diffusion in negligible, then the term d_i in Eq. (58) can be expressed according to Eq. (59):

$$d_i = \nabla X_i \tag{58}.$$

Since the diffusive mass flux vector is related to the diffusion velocity, as shown in Eq. (59):

$$J_i = \rho_i V_i \tag{59},$$

the Maxwell-Stefan equations can be written as shown in Eq. (60):

$$\sum_{j=1,j\neq i}^{N} \frac{X_i X_j}{D_{ij}} \left(\frac{J_j}{\rho_j} - \frac{J_i}{\rho_i} \right) = \nabla X_i - \frac{\nabla T}{T} \sum_{j=1,j\neq i}^{N} \frac{X_i X_j}{D_{ij}} \left(\frac{D_{T,j}}{\rho_j} - \frac{D_{T,i}}{\rho_i} \right) \qquad (60).$$

After some mathematical manipulations, the diffusive mass flux vector can be obtained from Eq. (61):

$$J_i = -\sum_{j=1,j\neq i}^{N-1} \rho D_{ij} \nabla Y_j - D_{T,i} \frac{\nabla T}{T} \qquad (61),$$

where D_{ij} are the terms of a (N-1)x(N-1) matrix *[D]*, computed according to Eq. (62):

$$[D] = [A]^{-1}[B] \qquad (62)$$

and *[A]* and *[B]* are (N-1)x(N-1) matrices, whose terms are computed as shown in Eqs. (63)÷(66):

$$A_{ii} = -\left(\frac{X_i}{D_{iN}} \frac{M_w}{M_{w,N}} + \sum_{j=1,j\neq i}^{N} \frac{X_j}{D_{ij}} \frac{M_w}{M_{w,i}} \right) \qquad (63),$$

$$A_{ij} = X_i \left(\frac{1}{D_{ij}} \frac{M_w}{M_{w,j}} - \frac{1}{D_{iN}} \frac{M_w}{M_{w,N}} \right) \qquad (64),$$

$$B_{ii} = -\left(X_i \frac{M_w}{M_{w,N}} + (1 - X_i) \frac{M_w}{M_{w,i}} \right) \qquad (65),$$

$$B_{ij} = X_i \left(\frac{M_w}{M_{w,j}} - \frac{M_w}{M_{w,N}} \right) \qquad (66).$$

The diffusive flux due to thermal gradients (Soret effect) is usually smaller than the flux related to concentration gradients, for this reason it has not been accounted for in the present work.

Fluent 6.0 has the capability to simulate heterogeneous chemical reactions, i.e. reactions occurring at the solid/fluid interface. The calculation of the species concentration at reacting surfaces is based on a balance of the convection and diffusion of each species to (or from) the surface and the rate at which it is consumed (or produced) at the surface.

Due to these features, Fluent 6.0 has been selected to perform detailed numerical simulations of the flow in the monolithic bed: the outcome of these simulations allow a verification of the

accuracy, reliability and limits of applicability of the simplified (lumped-parameters) model which has been developed in this work.

3.4 Distributed-parameters approach: the solution procedure

The Fluent 6.0 solver allows the numerical solution of the differential equations describing the flow of a viscous multi-component mixture of chemically reacting gases by means of different numerical methods. An implicit scheme has been selected to perform the simulations which will be presented in the next chapter: although such scheme requires a higher computational effort with respect to explicit methods, it is able to handle the high stiffness deriving from the coupling of the flow with a exothermic surface reaction. Please refer to [41] for further details on the solving procedure.

4. SIMULATION OF THE CATALYST FLOW

In this chapter, the predictive capabilities of the lumped-parameters model described in chapter 4 are assessed, through the comparison with experimental data and CFD simulations; examples of possible applications of the model as a support tool for the design and the optimization of a monolithic reactor for the heterogeneous decomposition of hydrogen peroxide solutions in space propulsive systems are presented.

4.1 Lumped-parameters simulations: preliminary results

The aim of this section is to present a sample of the data generated by the one-dimensional code which has been developed to numerically solve the lumped-parameters model equations.

As a first step, the code needs in input the concentration of the hydrogen peroxide solution (% weight) along with the flow rate and the initial temperature; geometrical features (cross section shape, cross section characteristic dimension, reactor length) are also assigned, as well as information about the catalytic activity (pre-exponential factor and activation energy), the operating pressure, the heat transfer model (i.e. constant wall heat flux or constant wall temperature, turbulent/laminar regime) and the final time to be reached during the simulation.

The code is able to simulate the flow inside a single monolith channel: a monolithic bed is actually made of several parallel channels, as shown in Fig. 17; anyway, if the peroxide is uniformly injected across the bed, the flow inside a single channel can be assumed to be representative of the flow across the whole reactor.

Figure 17. Monolithic bed

In order to run the code with realistic inputs, data available in literature [16] have been selected and are reported in Tab. 32.

Table 32. Input data for 1-D code (preliminary runs)

HTP grade (% weight)	87.5
Flow rate, kg/s	$1.67 \cdot 10^{-5}$
Cross section shape	Square
Channel dimension, m	$1.25 \cdot 10^{-5}$
Channel length, m	$1.50 \cdot 10^{-2}$
Initial temperature, K	323
Operating pressure, bar	2.5

The activation energy has been assumed to be equal to 50700J/mol, as reported in [42]: the pre-exponential factor has been set to $3 \cdot 10^4 \text{m} \cdot \text{s}^{-1}$: a constant heat flux Nusselt number has been considered, as suggested in [28, 43].

The 1-D code is able to predict the temporal and spatial evolution of the wall temperature and of the mean gas temperature (as well as of other variables, as the H_2O_2 concentration): the results corresponding to the input conditions summarized in Tab. 32 are shown in Fig. 18.
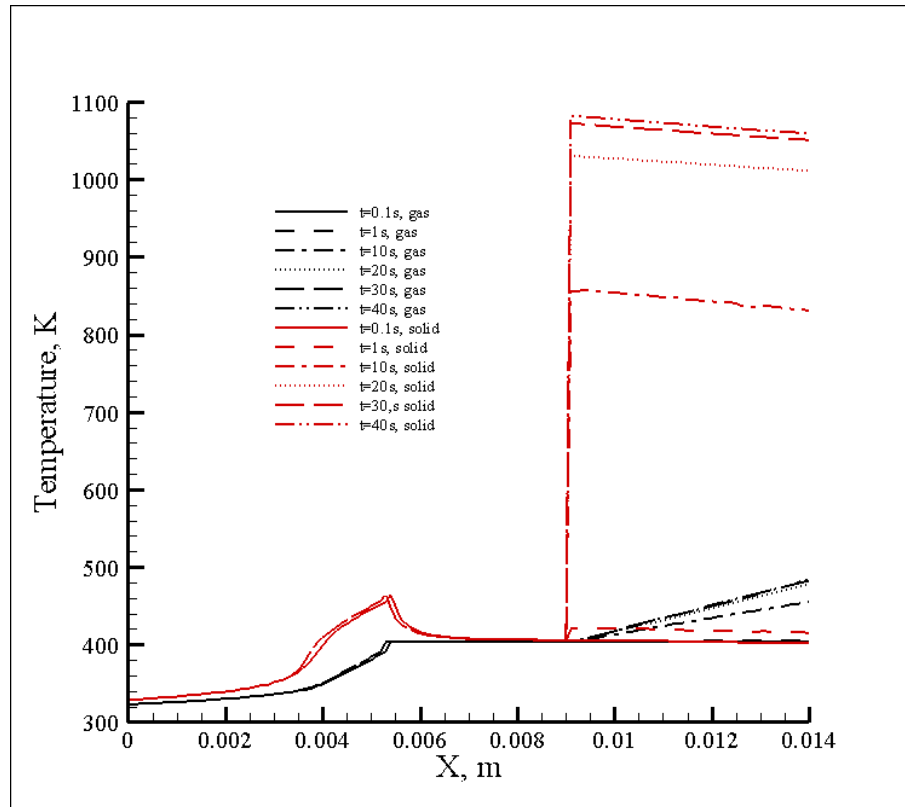

Figure 18. Temperature profiles along the monolith channel (temporal evolution)

56

Fig. 18 shows the existence of three different regions within the reactor: in the first one, extending roughly up to one third of the total monolith length, the liquid peroxide slowly decomposes and warms, up to the point where the boiling temperature of the solution is reached: in this condition, the fluid temperature remains constant and the heat which is released from further decomposition is used to vaporize the solution. During the evaporation process, the temperature at the solid/gas interface decreases: this behaviour is assumed to be due to the decrease in the reactant concentration on the wall, as a consequence of the strong density variation related to the transition from liquid to vapour. As stated in the previous chapter, a simplified description of the phase change has been embedded in the model: for this reason the extension of the constant-temperature region shown in Fig. 18 could be questionable. Nevertheless, these results could of course represent a conservative estimation of the length necessary to achieve full vaporization of the peroxide solution: such statement derive from the observation that the liquid/vapour equilibrium, which actually reduces the amount of liquid peroxide, is not accounted for in the present model. Furthermore, the model can be used to investigate the dependence of the length of the vaporization region on some reactor design parameters.

Once the solution has completely vaporized, the temperature starts to increase again gradually, up to the ignition point, where the wall temperature jumps to a much higher value (very close to the adiabatic decomposition temperature): as a consequence, the gas temperature begins to increase too.

Steady-state operations are achieved in almost 40s, as can be inferred from Fig. 19 too, where a comparison between the unsteady-model and the steady-model is shown: the gas-phase temperature profiles are very close, while a slight difference in the position of the ignition point exists. Such discrepancy is due to the errors associated to the discretization procedure: increasing the number of cells along the channel, the ignition point moves towards the reactor inlet (hence the error respect to the unsteady-model prediction decreases), as shown in Fig. 20. This behaviour can be explained according to the following considerations: the solid temperature is computed from the energy balance equation at the solid/fluid interface (i.e. Eq. (9) for the unsteady-model and Eq. (9') for the steady model); as steady conditions are achieved, the round-off errors associated to the numerical solution of Eq. (9) go to zero, which means that the predicted temperature tends to the exact value; on the other side, only an approximate solution to the non-linear algebraic Eq. (9') can be computed by means of iterative methods, as reported in the previous chapter.

The influence of the time discretization has been also verified: as shown in Fig. 21, a loss of accuracy can result from too large time steps; eventually, instabilities can occur.
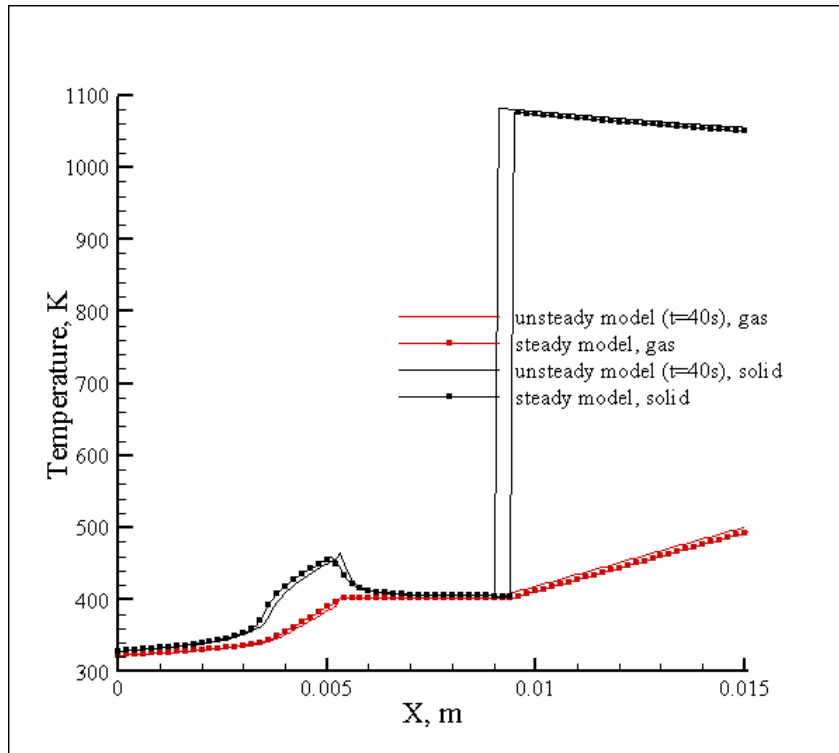

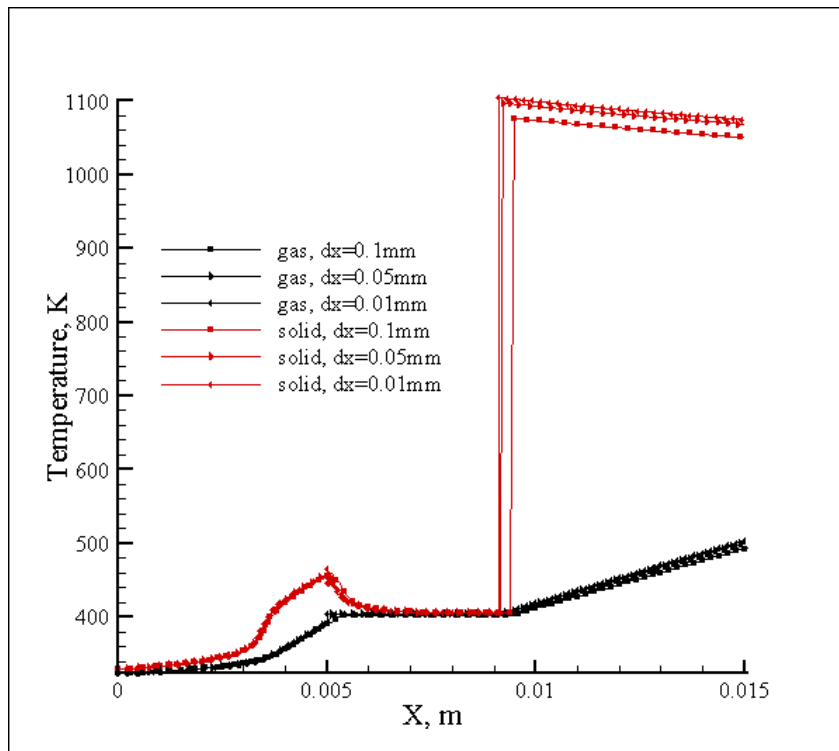**Figure 19. Temperature profiles along the monolith channel (unsteady-model vs steady-model predictions)**

Figure 20. Temperature profiles along the monolith channel (influence of spatial discretization)
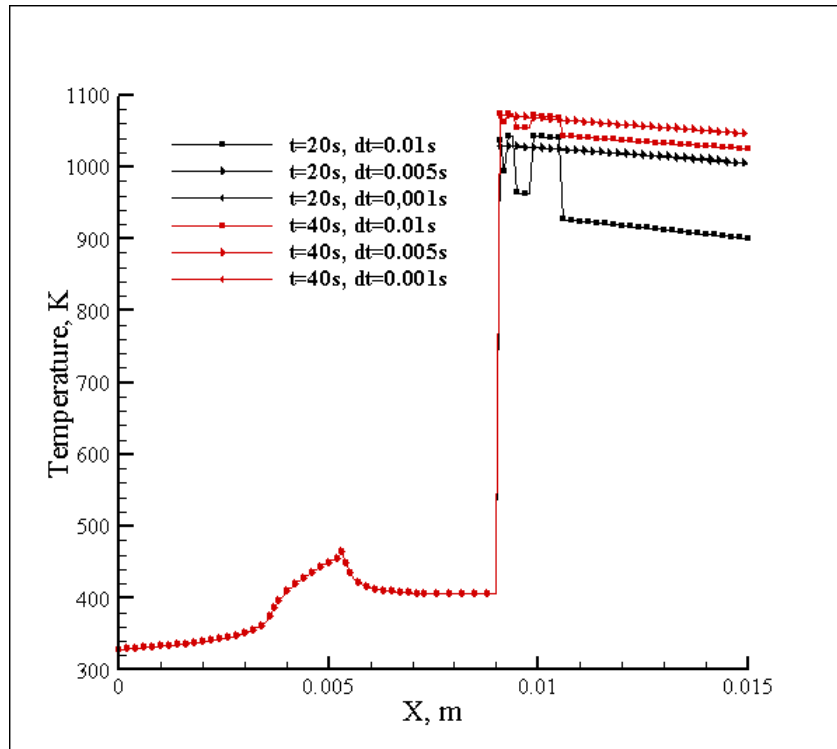
Figure 21. Solid temperature profiles along the monolith channel (influence of time discretization)

4.2 Lumped-parameters predictions: comparison with experimental data

The analysis of monolithic beds performances in space propulsive systems is a recent topic, hence few data on the experimental characterization of such systems are available in literature: moreover, only global measurements (i.e. chamber operating pressure, engine thrust or specific impulse) are often reported, with no clear specification of the testing conditions (which means that no inputs are available to perform numerical simulations).

The only work (according to the knowledge of the author of the present thesis) which allows a comparison of numerical predictions and experimental data has been recently presented by Scharlemann et al. [16]. Monolithic beds, obtained using two different ceramic supports (see Tab. 33 for details) have been used to decompose HTP solutions (grade: 87.5 % weight) in the operating conditions representative of application on micro-thrusters (the target design performances are summarized in Tab. 34).

Table 33. Monolithic supports used in Ref. [16]

Support material	Cells per square inch	Number of channels	Length	Rectangular cross section
Mullite	223	6x6	13.6mm	$10.2x10.3mm^2$
Mullite-zirconia	273	6x6	15.5mm	$9.1x9.5mm^2$

Table 34. Target performances for a HTP-based micro-thruster (Ref. [16])

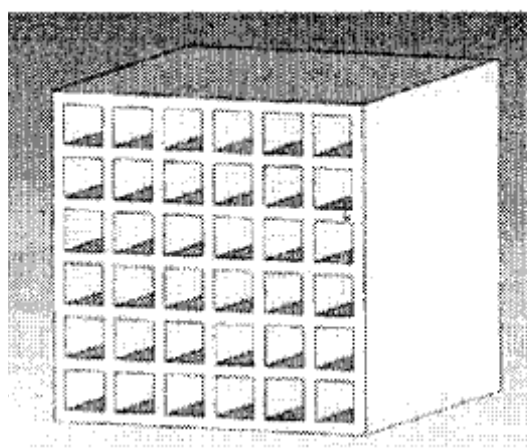|	Design values
Thrust, mN	100÷500
Specific impulse, s	140÷180
Mass flow rate, g/s	0.055÷0.036
ΔV, m/s	50÷300
Life-time, hours	~16

Figure 22. Schematic drawing of the monolithic bed tested in Ref. [16]

As can be inferred from Tab. 33 and from Fig. 22, the catalytic reactor is composed of multiple square section channels: the injection plate provides the homogeneous distribution of the HTP mass flow rate into each channel (the plate has 36 holes with a diameter of 0.1mm). This configuration allows the extrapolation of the flow condition inside each channel (just scaling the flow rate by a factor of 36) and hence the simulation of the flow in a single channel.

Following this procedure, the operating conditions which have been previously reported in Tab. 32 have been obtained.

As reported in [16], the temperature at the exit section of the monolithic bed has been measured during the tests: a first comparison between the experimental tests and the predictions of the lumped-parameters model is shown in Fig. 23.

Two major discrepancies are evident: firstly, in the numerical simulation the transition from the liquid to the gas phase occurs in a very short time and no liquid is ejected from the monolith outlet also at the beginning of the test, while the measurements demonstrate the existence of liquid HTP exiting the bed for a longer period (as the temperature remains approximately constant and below the boiling value for about 6s).
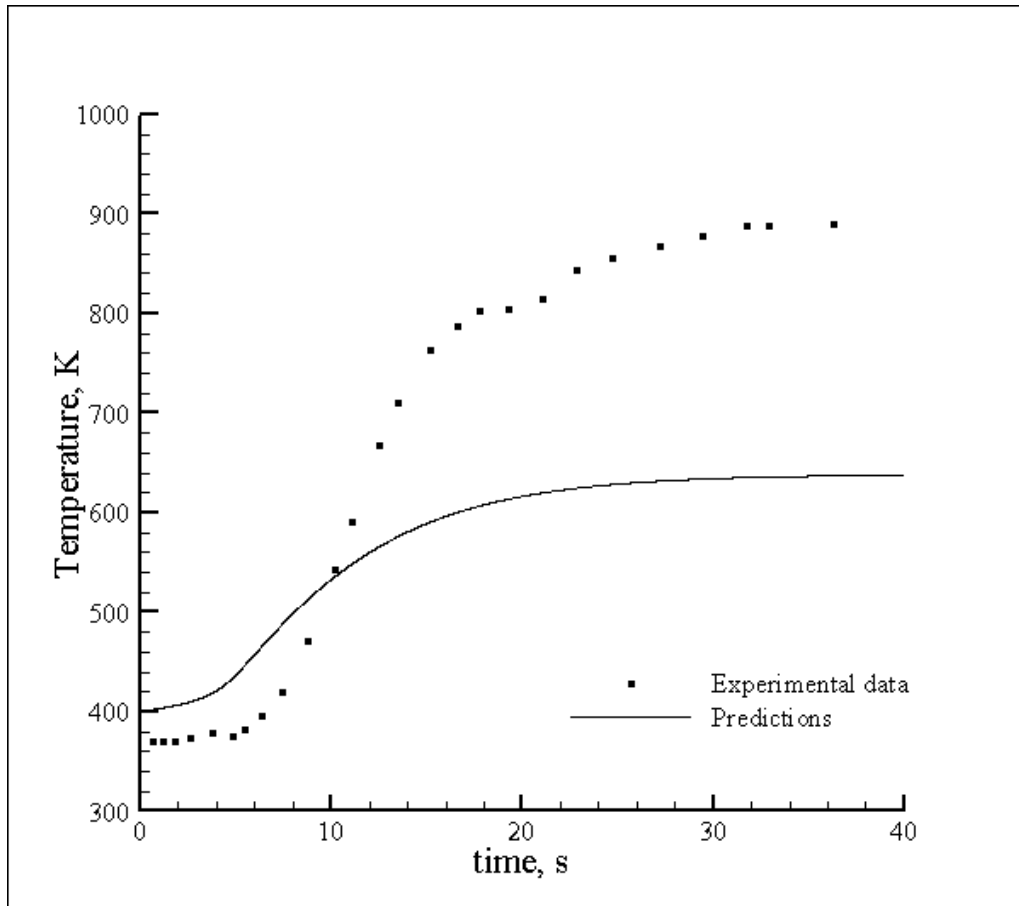
Figure 23. Temperature profile at the exit section of the monolithic bed: experimental data and predictions (laminar heat and mass transfer)

This difference is partially due to the simplified assumptions embedded in the model: the unsteady behaviour of the solid/fluid system is assumed to be dominated by the thermal properties of the solid, hence the thermal capacity of the fluid is neglected; as stated in chapter 4, this assumption does not affect the accuracy of the results when the reacting mixture is in gaseous phase, but errors can arise when the HTP is still a liquid. Furthermore, during the experimental tests a delay between the passage of the peroxide in the feeding line and the starting of the decomposition process occurs, due to the length of the feeding line itself. This delay should artificially be accounted for in the numerical simulations too, just shifting the starting time of the simulation of a certain Δt.

Secondly, the final steady-state temperature which is reached in the numerical simulations (~600K) is smaller than the value measured during the test (~900K, which is very close to the adiabatic decomposition temperature): this difference has proved to be due to the hypothesis of laminar flow throughout the whole reactor, which has been assumed in the first numerical tests.

Indeed the evaluation of the Reynolds number profiles inside the channel (see Fig. 24) shows that once the reactants have completely vaporized, Re~3500: this value is greater than the threshold which is usually considered for the laminar/turbulent transition (Re=2300, as reported in [44]).
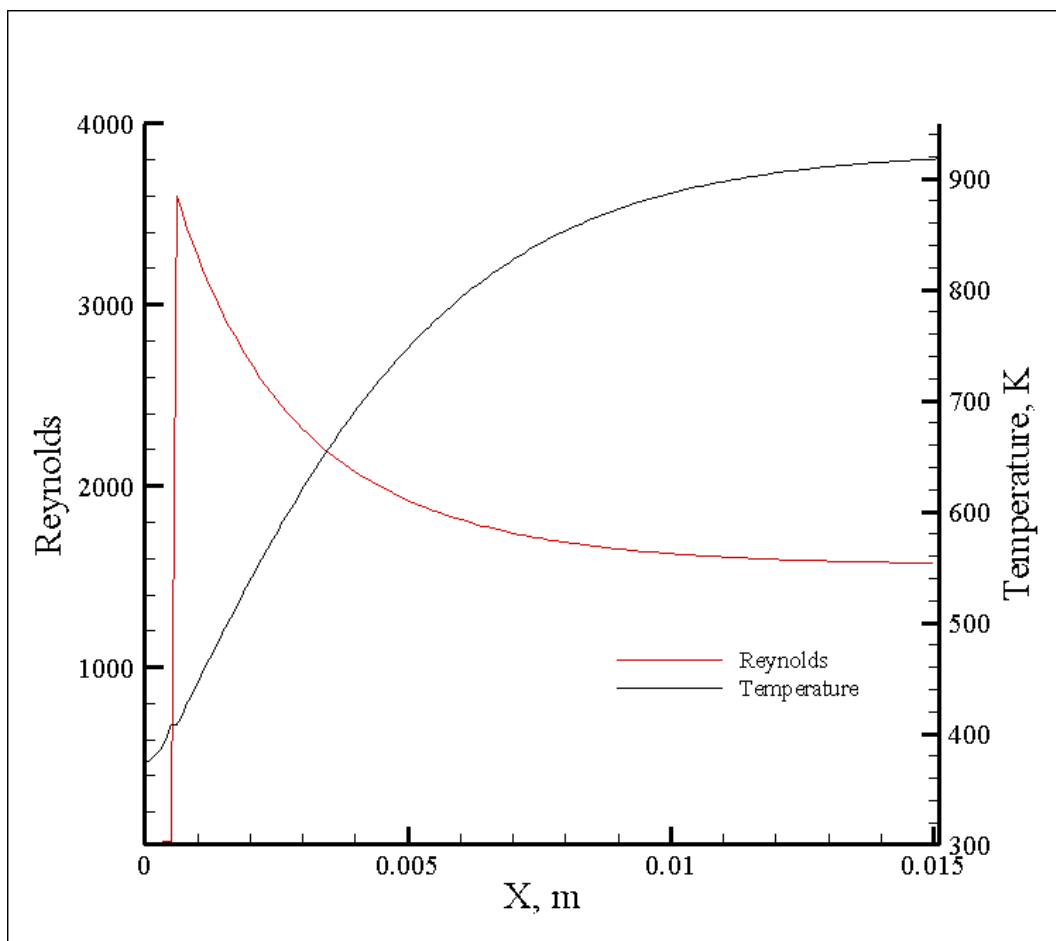

Figure 24. Temperature and Reynolds number profiles along the monolithic bed

Hence new runs assuming a turbulent regime (which means that higher values of the Nusselt and Sherwood numbers have been considered to account for the increased heat and mass transfer rates due to the turbulence, as reported in the previous chapter) have been performed: the final temperature is closer to the experimental data, as shown in Fig. 25.

The 1-D model under-predicts the induction time, which is approximately equal to 20s, while a higher value (about 30s) can be inferred from the experimental data.
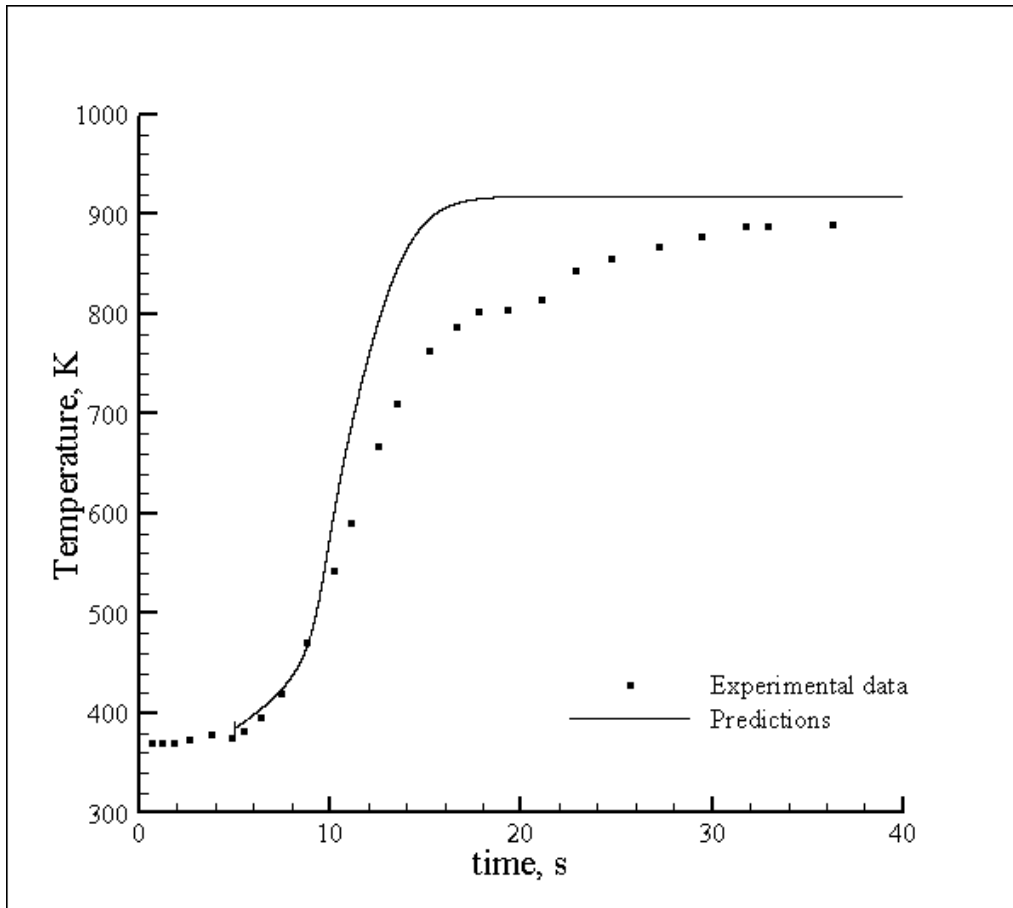
Figure 25. Temperature profile at the exit section of the monolithic bed: experimental data and predictions (turbulent heat and mass transfer)

The authors of the experimental tests have also performed additional measurements at a higher operating pressure (6bar): as shown in Fig. 26, a good agreement between the predictions and the experimental data holds in this condition too.

The temperature rise is completed within a shorter time (about 15s) with respect to the case at lower pressure: this is due to the increased density of the vapour phase as a consequence of the increased pressure, which results in a higher hydrogen peroxide concentration.

In Fig. 27, a comparison between the temperature profile at both pressures (2.5bar and 6bar) is reported.
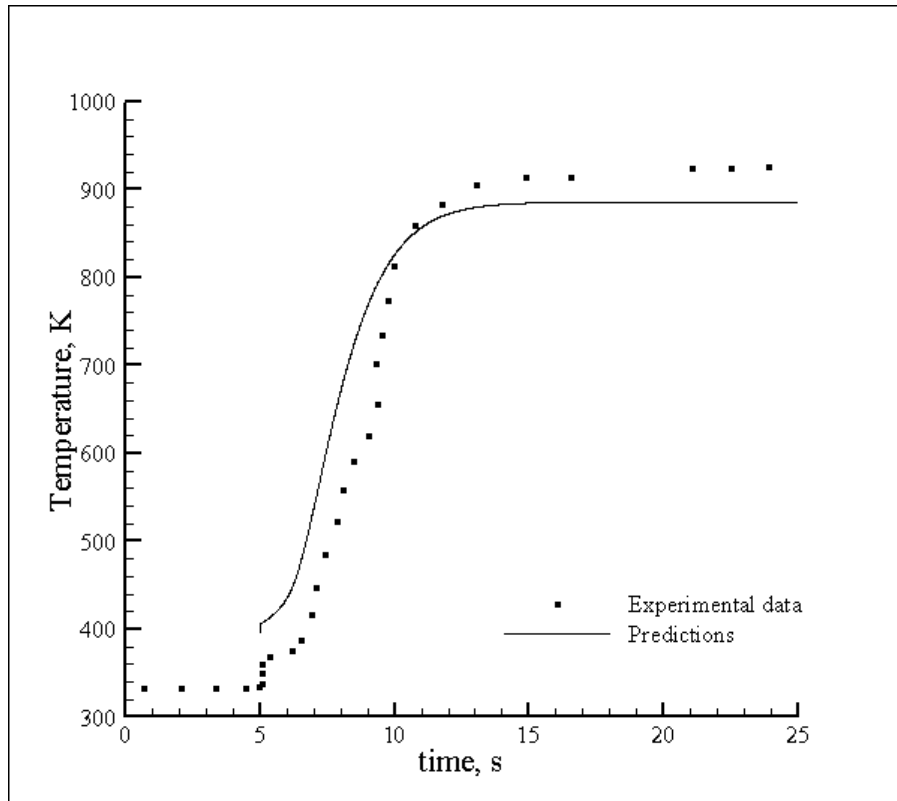
Figure 26. Temperature profiles at the exit section of the monolithic bed: experimental data and predictions (operating pressure: 6bar)
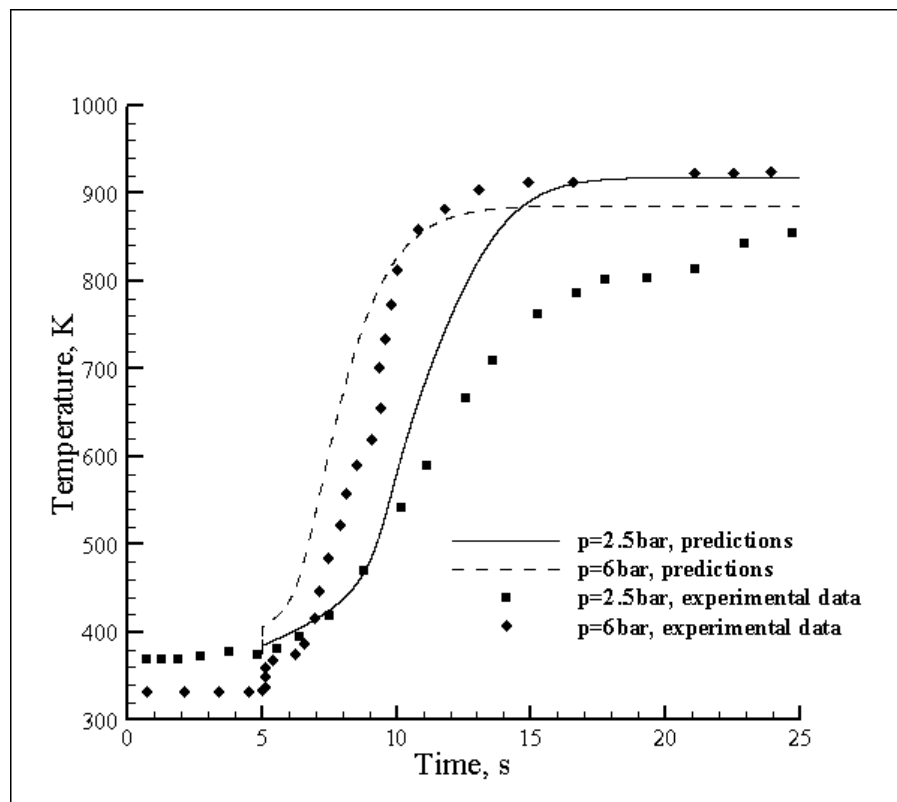

Figure 27. Temperature profiles at the exit section of the monolithic bed: experimental data and numerical predictions (influence of the operating pressure)

64

4.3 Lumped-parameters predictions: comparison with CFD simulations

In the previous paragraph, the accuracy of the 1-D code has been assessed through the comparison with experimental data: the code has proved to be able to correctly reproduce the measured trends (with major emphasis on the induction time and the decomposition temperature).

In this section further assessment of the predictive capabilities of the simplified model is presented, with particular attention to the prediction of the ignition point: as stated in chapter 3, a correct evaluation of the ignition abscissa is *conditio sine qua non* to achieve a correct sizing of the reactor.

The CFD solver Fluent 6.0 has been used to perform detailed numerical simulations of the flow inside the monolith channel: details on the modelling and solution strategies which have been accounted for have been reported in the previous chapter.

The results of the CFD simulations are assumed as a reference to evaluate the accuracy of the predictions of the simplified model.

In order to reduce the computational effort required by each CFD run, only steady-state computations have been carried out: for this reason, the 1-D steady code has been used.

The equivalence between the 1-D steady and the 1-D unsteady predictions has been assessed formerly in this chapter.

As a first step, a grid analysis has been carried out, to assess the impact of the numerical discretization on the CFD predictions: the input conditions are as reported in Tab. 35. The following assumptions should be pointed out:

a) the reactants are assumed to enter the channel in vapour phase: this condition is determined by the capabilities of the CFD solver, which is not able to model a multi-phase fluid with a heterogeneous chemical reaction;

b) the temperature, the velocity and the mass fraction of the species entering the reactor (hydrogen peroxide, water and oxygen) at the inlet section of the reactor are computed using the simplified model: the values corresponding to the complete vaporization of a solution having the initial grade and temperature reported in Tab. 35 are used;

c) the flow is assumed to be laminar in the whole reactor: this assumption is due to the selected mass flow rate which is one order of magnitude smaller than the one considered in the previous section (hence the Reynolds number will not reach the threshold value for transition to the turbulent regime).

Table 35. Inputs for CFD simulations (grid analysis)

Mass flow rate, kg/s	10^{-6}
HTP grade, % weight	100%
Inlet temperature, K	300
Outlet pressure, bar	1
Pre-exponential factor, m·s^{-1}	500
Activation energy, J·mol^{-1}	44100
Cross sectional shape	circular
Channel diameter, m	0.001
Channel lenght, m	0.015

The channel is assumed to have a circular cross section: as a consequence, the flow can be considered axis-symmetrical.

The results of the grid analysis are reported in Figs. 28 and 29: the grid spacing along the radial coordinate has a strong influence on the position of the ignition point (doubling the number of cells from 20 to 40, a large shift of about 2 millimiters towards the reactor inlet occurs); the grid spacing along the axial coordinate seems to have a smaller impact (a four-fold increase in the number of cells from 150 to 600 results in a shift towards the reactor outlet of less than 1 millimeters).
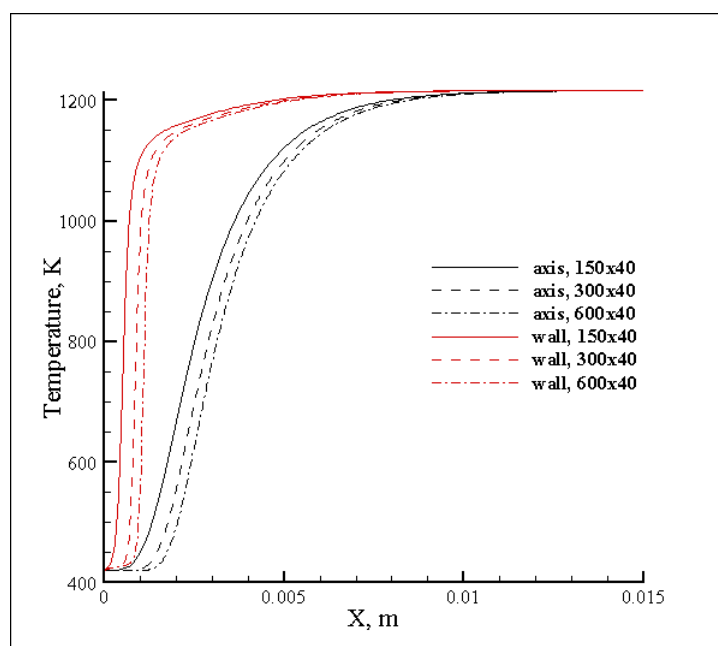

Figure 28. Temperature profiles along the monolith channel (influence of the grid spacing along the axial coordinate)
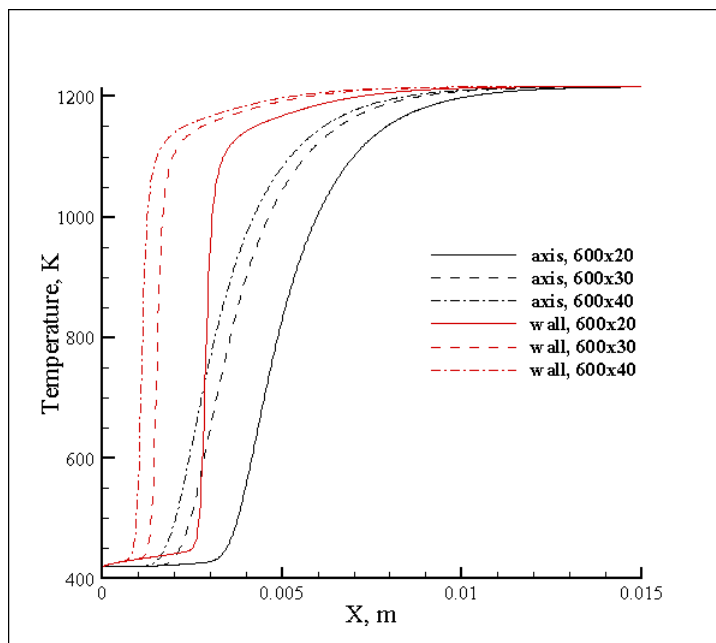
Figure 29. Temperature profiles along the monolith channel (influence of the grid spacing along the radial coordinate)

The impact of the numerical scheme has been also investigated: fixed the number of cells, an increase in the accuracy of the scheme (from the first to the second order) produces a shift of the ignition point towards the reactor outlet (as shown in Fig. 31). This effect is similar to the one corresponding to an increase in the number of cells along the axial coordinate.
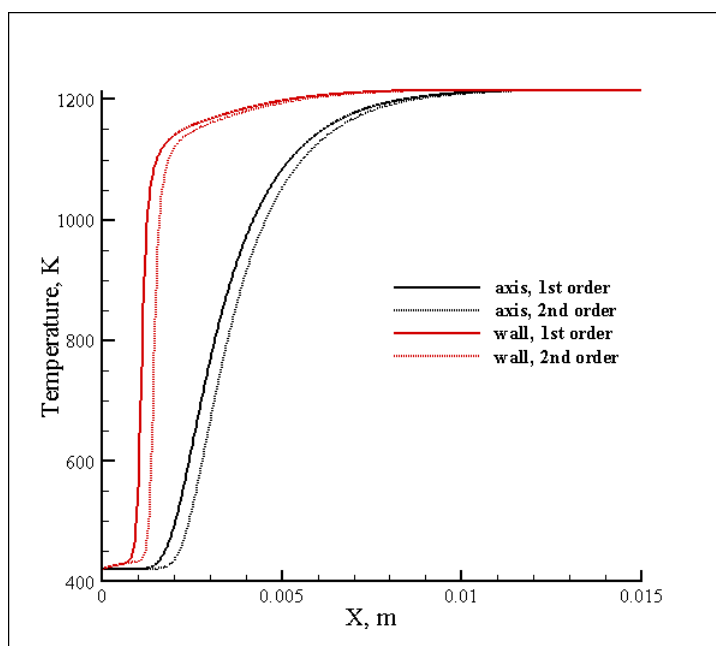

Figure 30. Temperature profiles along the monolith channel (influence of the numerical scheme)

The influence of the inlet boundary conditions has been assessed too: the difference between a plug-flow assumption (i.e. a uniform velocity profile at the inlet) and a parabolic profile (corresponding to a fully laminar flow) is reported in Fig. 31.

As expected, the ignition point largely shifts towards the reactor inlet: this effect is due to the decrease of the heat and mass transfer rates with respect to the plug-flow case.

This trend can be correctly reproduced by the simplified model too: please recall the shape of the heat generation and the heat removal curves shown in chapter 3, along with the considerations on the steady-state temperature which is determined by the intersection of such curves.

 The heat transfer coefficient corresponds to the slope of the heat removal curve: if the heat transfer decreases (keeping the other parameter constant), the slope decreases too, up to the point where an additional intersection with the heat generation curve occurs (see Fig. 32); in this condition, the wall temperature jumps to the solution on the right side of the heat generation curve.
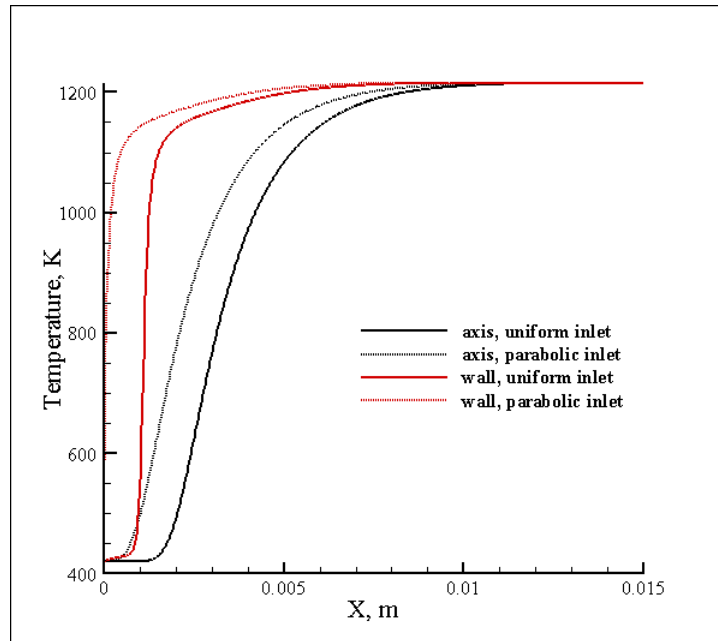

Figure 31. Temperature profiles along the monolith channel (influence of the inlet boundary condition)
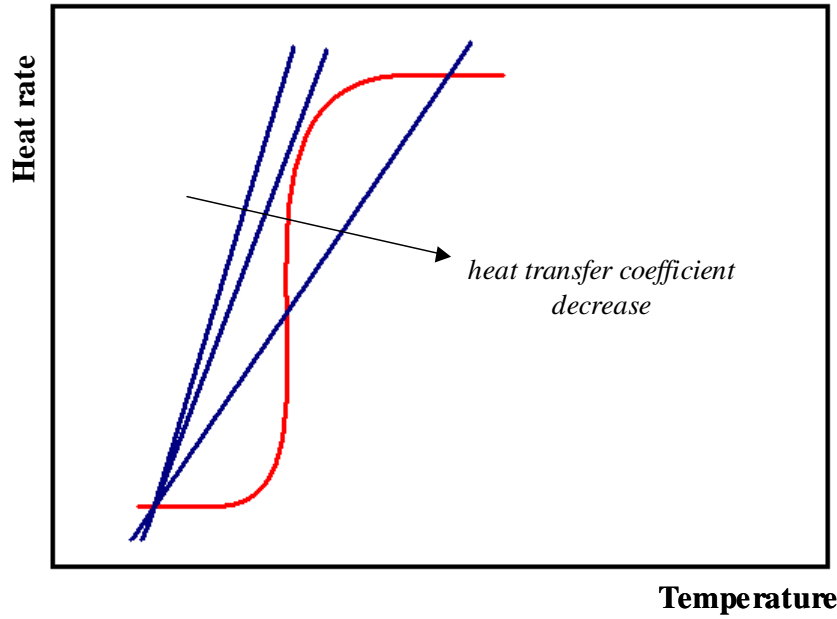
68

Figure 32. Heat generation curve (red) and heat removal curve (blue) vs temperature (influence of the heat transfer coefficient)

As the velocity profile in a real monolithic bed is expected to be close to the plug-flow inlet, such boundary condition is considered hereinafter in this work.

Once the grid analysis has been carried out, the results of the CFD simulations and the predictions of the simplified model have been compared, assuming the reactor inlet conditions previously reported in Tab. 35.

The constant-pressure assumption embedded in the 1-D code has proved to be fully verified in the selected operating conditions: the pressure drop within the reactor is negligible, as shown in Fig. 33.

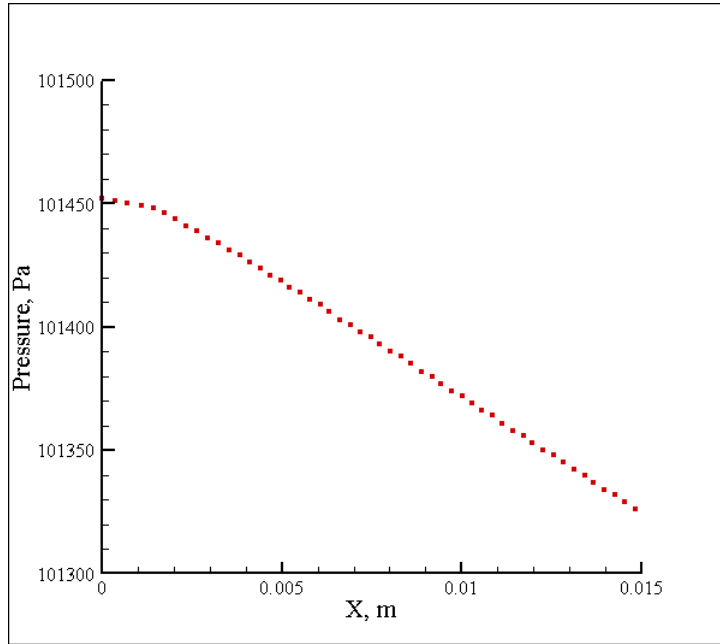**Figure 33. Pressure profile along the monolith channel**
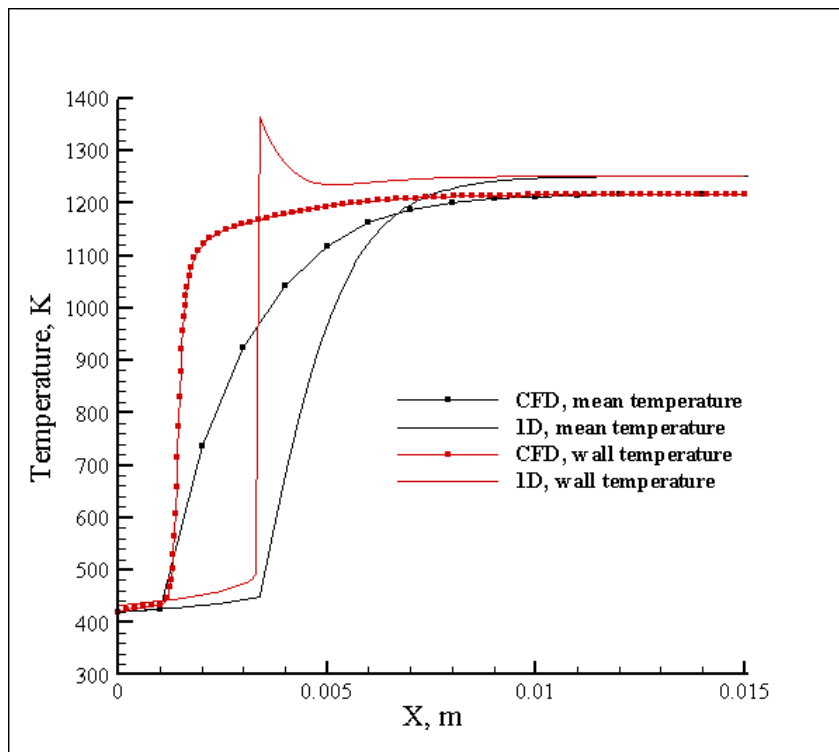

Figure 34. Temperature profiles along the monolith channel (CFD simulations and 1-D predictions, axis-symmetric case, initial HTP grade: 100% weight, mass flow rate: 10^{-6} kg/s)
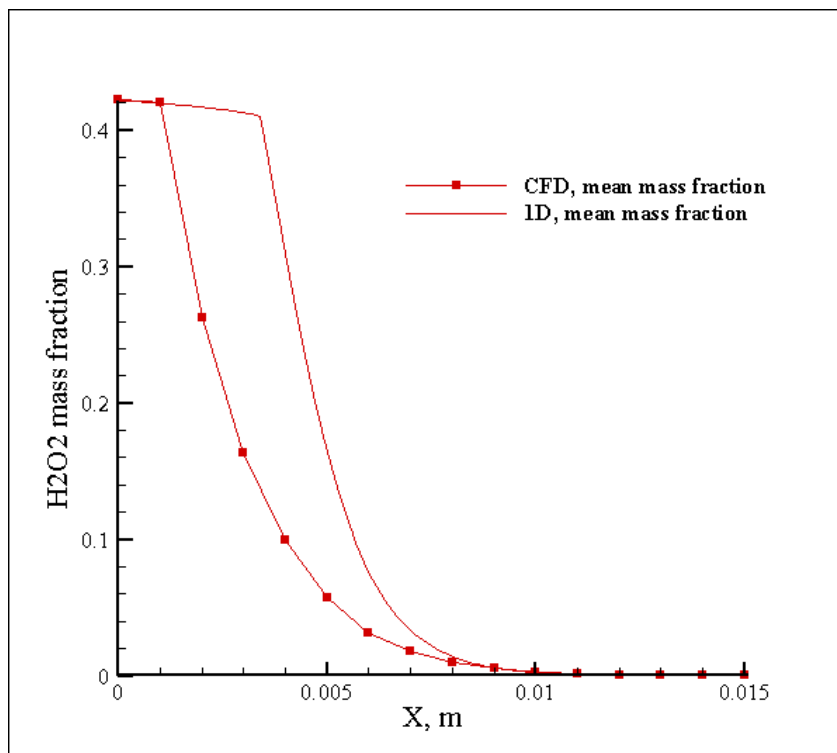
Figure 35. H$_2$O$_2$ mass fraction profiles along the monolith channel (CFD simulations and 1-D predictions, initial HTP grade: 100%, , mass flow rate: 10^{-6} kg/s)

Figs. 34 and 35 shows that both the detailed and the simplified model predict that the ignition will occur within the reactor: a discrepancy exists in the position of the ignition point, which is respectively about 1mm and 3mm downstream the reactor inlet in the CFD simulations and the 1-D predictions. According to both models, complete conversion of the peroxide occurs (see Fig. 36) and the final temperature is close to the adiabatic value: the 1-D code shows that a peak in the wall temperature occurs close to the ignition point, with an over-shoot of about 8% with respect to the final temperature. This behaviour, which is not predicted by the CFD solver, is assumed to be due to the simplified modelling assumptions embedded in the lumped-parameters tool.

The input conditions summarized in Tab. 35 have been modified to further assess the accuracy of the 1-D model.

Firstly, the initial hydrogen peroxide grade has been decreased to 85% weight: in this condition, according to both models the ignition does not occur in the selected domain, as can be inferred from Figs. 36 and 37. The peroxide concentration remains approximately constant and the temperature rise is less than 10K, as shown in Fig. 38.
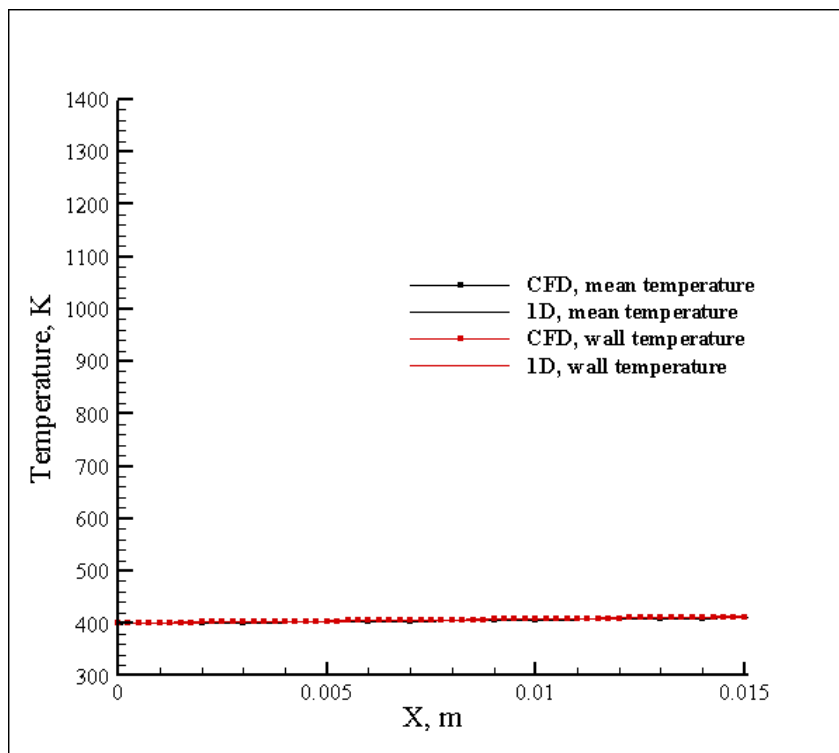
71

Figure 36. Temperature profiles along the monolith channel (CFD simulations and 1-D predictions, initial HTP grade: 85% weight)
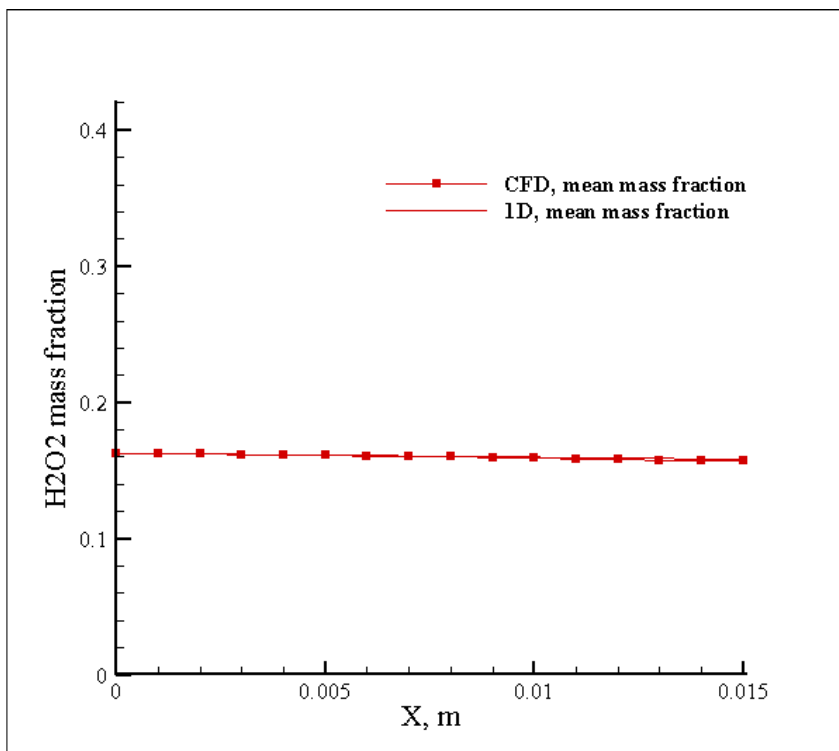

Figure 37. H_2O_2 mass fraction profiles along the monolith channel (CFD simulations and 1-D predictions, initial HTP grade: 85% weight)

Figure 38. Temperature profiles along the monolith channel, zoom (CFD simulations and 1-D predictions, initial HTP grade: 85%)

Secondly, the mass flow rate within the reactor has been increased, as reported in Tab. 36: a ten-fold increase in the catalyst activity has been considered too, in order to keep the Damkholer number (which represents the ratio of the chemical time-scale to the fluid-dynamic time scale) constant.

Table 36. Inputs for CFD/1-D simulations

Mass flow rate, kg/s	10^{-5}
HTP grade, % weight	100%
Inlet temperature, K	300
Outlet pressure, bar	1
Pre-exponential factor, m·s^{-1}	5000
Activation energy, J·mol^{-1}	44100
Cross sectional shape	circular
Channel diameter, m	0.001
Channel length, m	0.015

Despite the higher flow rate, the constant-pressure assumption is still valid: the total pressure drop is less than 1%, as shown in Fig. 39.
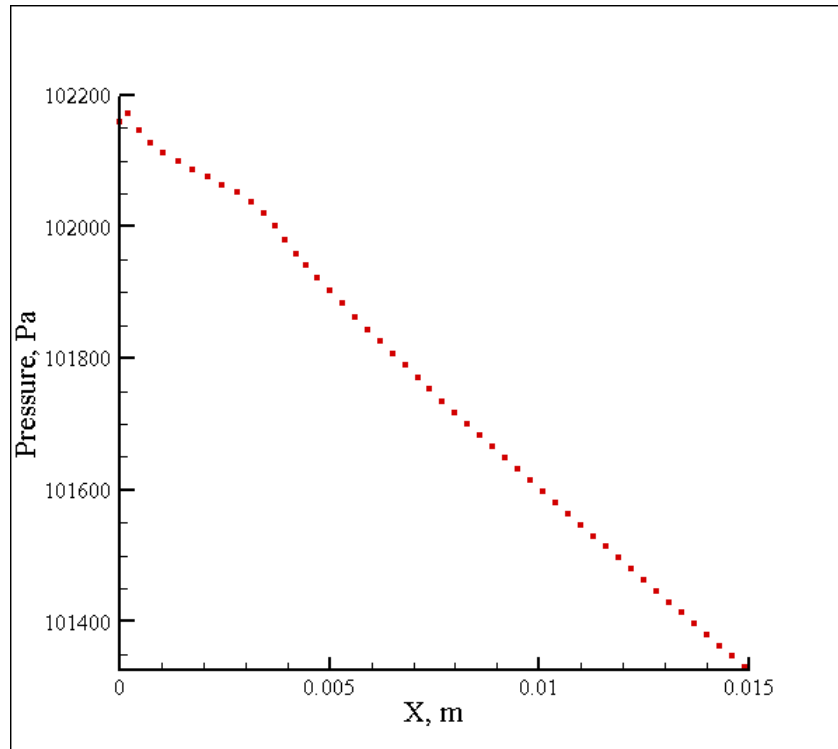
Figure 39. Pressure profile along the monolith channel

As the Reynolds number at the inlet section is above the threshold value for the laminar/turbulent transition, a full turbulent flow has been assumed: the *k-ω* model has been used for the CFD simulation.

As shown in Figs. 40 and 41, the 1-D predictions are in reasonable agreement with the CFD results in this case too.

Both models predict the ignition within the selected domain; anyway no complete conversion is achieved and a certain fraction of hydrogen peroxide is still present in the mixture exiting the reactor.
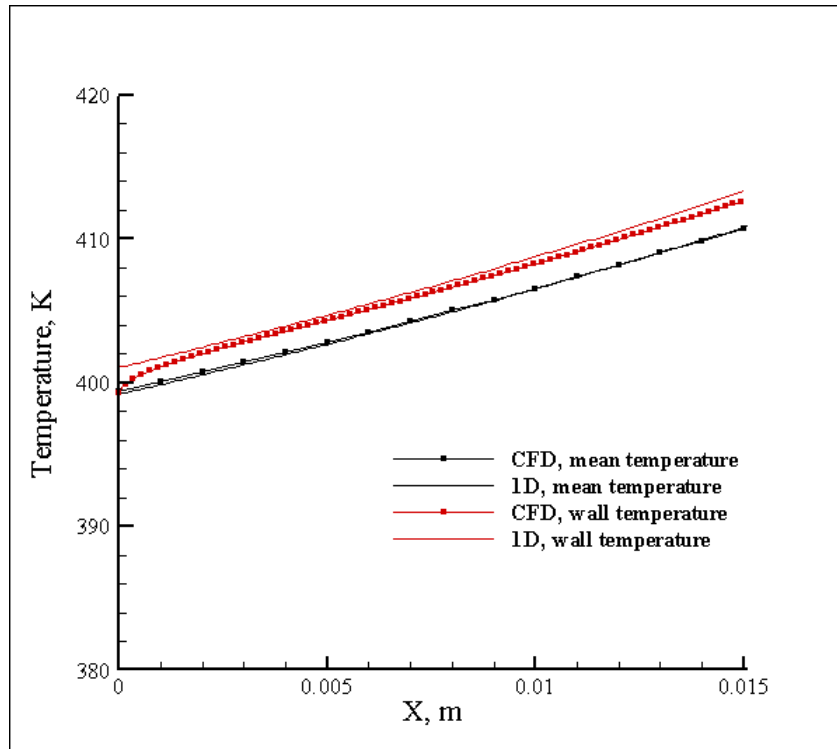
Figure 40. Temperature profiles along the monolith channel (CFD simulations and 1-D predictions, initial HTP grade: 100%, , mass flow rate: 10^{-5} kg/s)

Figure 41. H_2O_2 mass fraction profiles along the monolith channel (CFD simulations and 1-D predictions, initial HTP grade: 100%, , mass flow rate: 10^{-5} kg/s)

75

Before moving to the next section, some final remarks on the comparison presented above are worthwhile: the simplified model which has been devel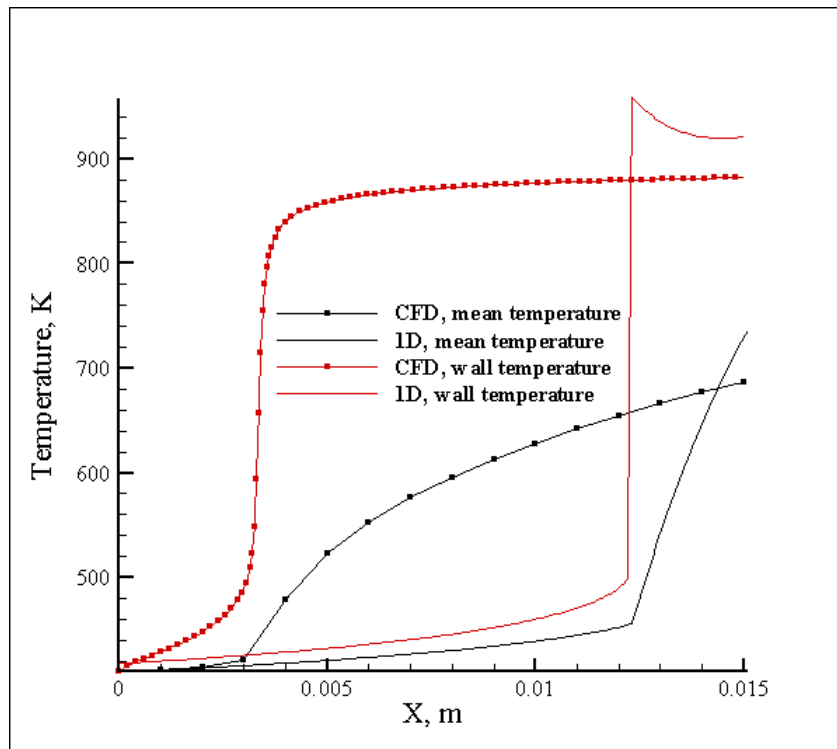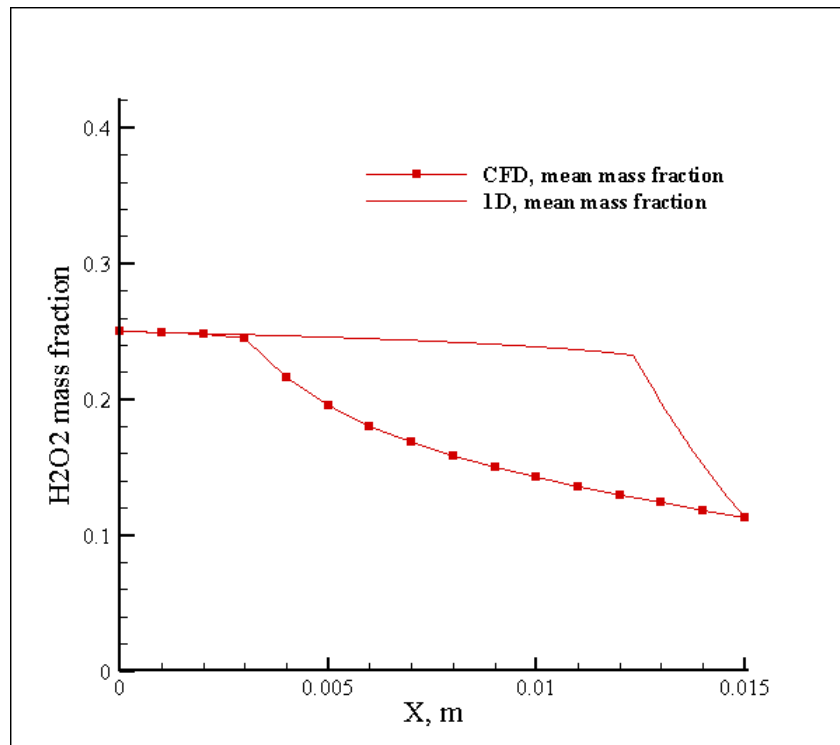oped in the present work has proved to correctly reproduce the behaviour predicted by means of CFD simulations; such agreement holds in a wide fraction of the operating envelope in which a reactor for the decomposition of hydrogen peroxide solutions in space propulsive systems will likely work.

A major difference arises, when considering the time necessary to obtain such predictions: the results of the 1-D code are obtained in real-time, while each CFD run requires a much larger effort (up to 40 hours for the 2-D simulations considered in the present work).

The possibility to screen in a very short time several different configurations has a straightforward importance for any predictive tool to be used as a support to the design.

4.4 Lumped-parameters model: applications

In the preceding paragraphs, the accuracy and the reliability of the lumped-parameters model have been assessed against experimental data and detailed numerical simulations: let now move to the utilization of such model to evaluate the performance of the monolithic reactor in different cases, i.e. when no experimental data are available and/or detailed numerical predictions (as CFD simulations) can not be attained in reasonable time.

Firstly, let consider a channel with a square cross section: this is a three-dimensional geometry, whose simulation by means of CFD-based techniques would require a computational effort up to one/two weeks (this value has been extrapolated from the data which have been obtained in the present work for 2-D simulations, just assuming a ten-fold increase in the size of the computational grid).

The comparison between the temperature profiles in a circular and in a square channel is shown in Fig. 42 (the input conditions reported in Tab. 35 have been assumed): an earlier ignition occurs in the 3-D case but, due to the lower heat and mass transfer coefficients with respect to the axis-symmetrical case, the mean temperature rises slowly and this behaviour finally turns in a lower efficiency of the reactor.
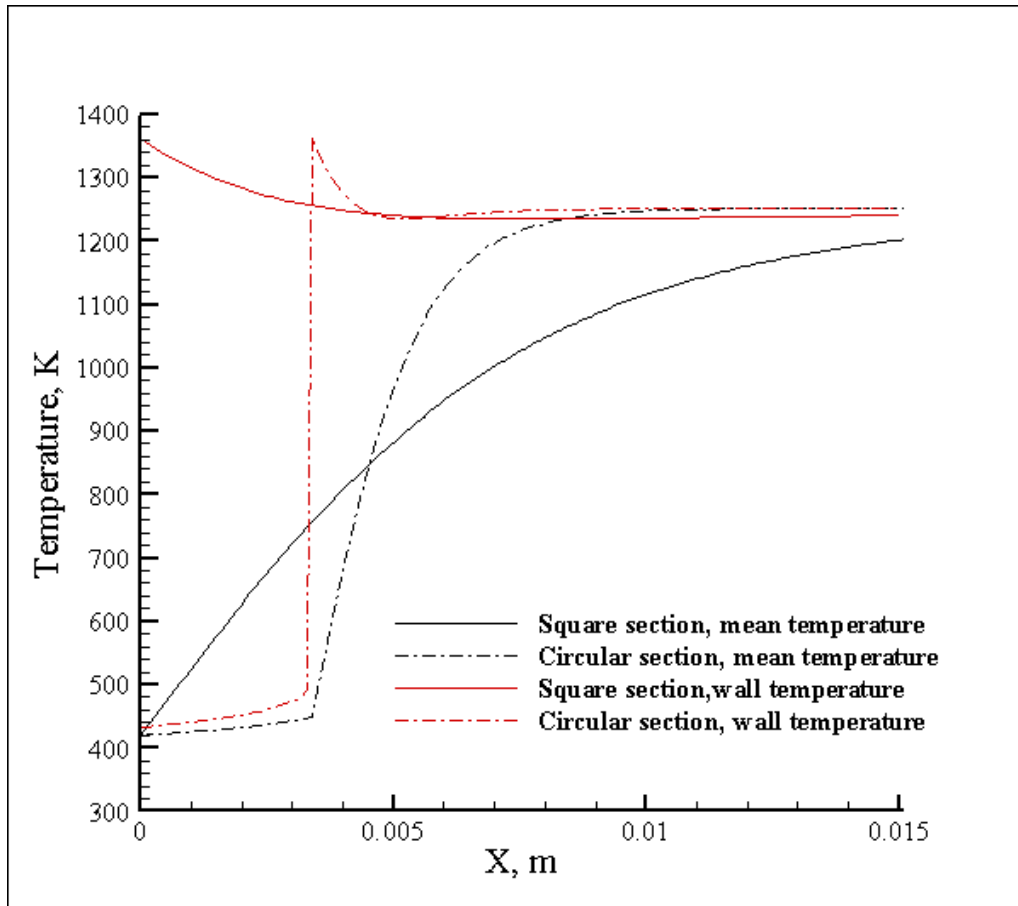
Figure 42. Temperature profiles along the monolith channel (comparison between circular and square section)

Secondly, let come back to the configuration which has been experimentally investigated in [16] and has been previously presented in this chapter: now the effect of different design variables can be evaluated, in order to identify the most effective ways to improve the reactor performances. As expected, one of the most important parameter to control the transient behaviour of the reactor is the density of the catalytic material: as shown in Fig. 43, halving the density of the catalytic material from $2800 kg/m^3$ (the value is referred to mullite) to $1400 kg/m^3$ (which could be easily attained for ceramic foams [45]) a three-fold reduction of the induction time (from about 15s to 5s) is obtained.
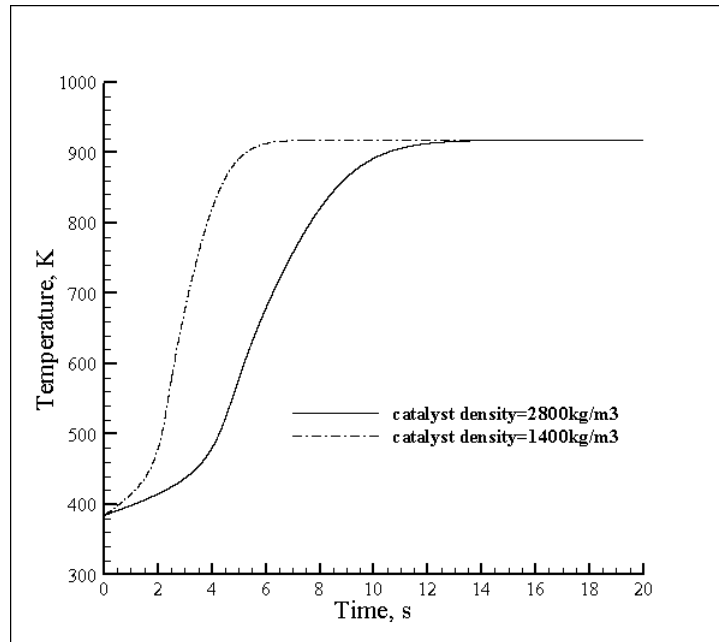
Figure 43. Temperature profile at the exit section of the monolith channel (influence of the catalyst density)

Another parameter which affects the time response of the reactor is the diameter of the channel: keeping constant the mass flow and halving the channel diameter, a reduction of the induction time from 15s to 10s is obtained, as reported in Fig. 44.

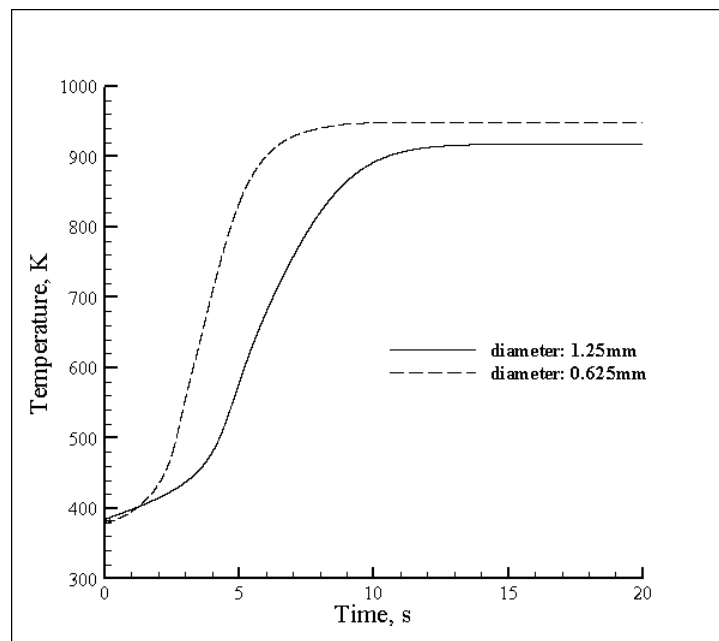**Figure 44. Temperature profile at the exit section of the monolith channel (influence of the channel diameter)**

The faster response time obtained with the smaller channels can be explained considering that the efficiency of the decomposition reaction on the catalyst wall increases as the surface to volume ratio increases. The reduction in the channel size has also a positive impact on the reactor volume necessary to have a high conversion rate, as shown in Fig. 45 (a ten-fold decrease in the channel diameter has been considered in this case, while the mass flow is kept constant). As the size of the channel decreases, the ignition point moves towards the reactor inlet: this means that if the bed total cross section area is kept constant too, a shorter and lighter reactor can be used to obtain the same thrust.

Figure 45. Temperature profile along the monolith channel (influence of the channel size, mass flow: 10 kg m^{-2} s^{-1})

Let consider a ten-fold increase in the mass flow rate: as a consequence, the mass flow grows from the value close to $10 kg\, m^{-2}\, s^{-1}$ which has been considered for the previous cases to $100 kg\, m^{-2}\, s^{-1}$. Fig. 46 shows that the 1.25mm channel is not able to handle this higher value, while full conversion is achieved with the 0.125mm channel.

This means that, keeping the bed total cross section area constant, a ten-fold decrease in the channel size allows a ten-fold increase in the total achievable thrust.

A parameter which is frequently used to evaluate the efficiency of the catalytic bed is the catalyst bed loading, which incidentally is defined just at the total mass flow across the reactor. Values in

the range $60 \div 235 \text{kg} \cdot \text{m}^{-2} \cdot \text{s}^{-1}$ have been reported for traditional packed beds, with the lower value referred to cold starts [13].

As shown in Fig. 46, the performances of a monolithic bed are at least comparable with that of a packed bed for the cold start case, as a bed loading equal to the threshold value reported above can be easily achieved: further works reported in literature demonstrate that monoliths can withstand bed loadings up to $300 \text{kg} \cdot \text{m}^{-2} \cdot \text{s}^{-1}$ [50].
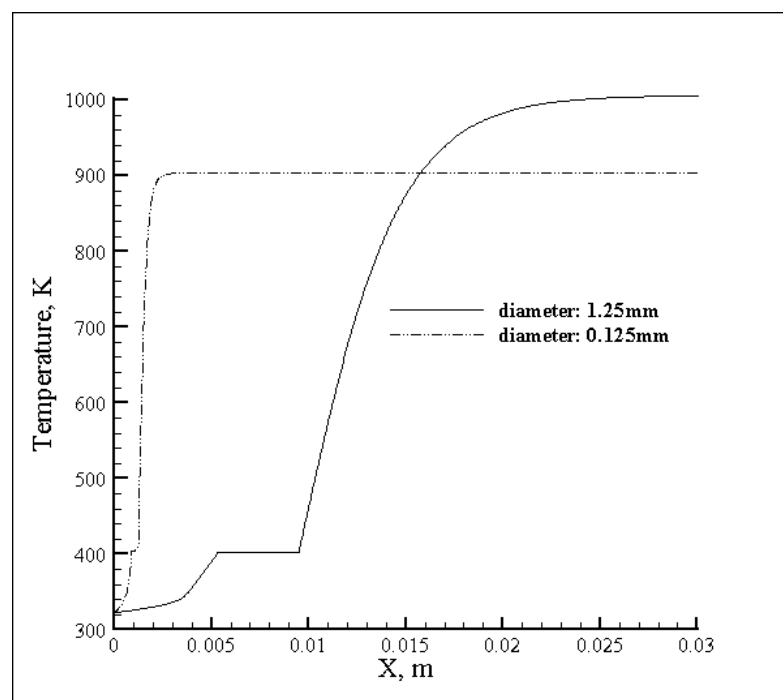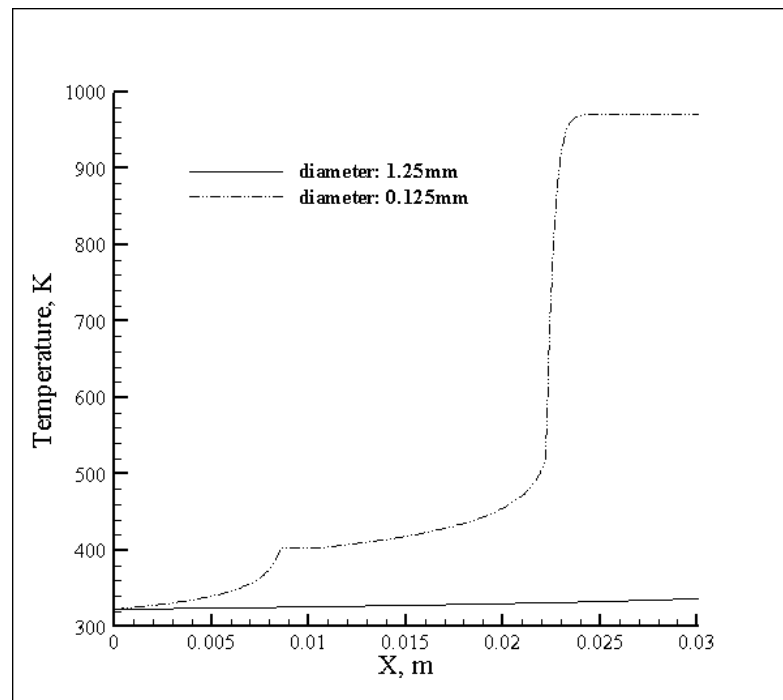

Figure 46. Temperature profile along the monolith channel (influence of the channel size, mass flow: 100 kg $\cdot$ m^{-2} s^{-1})

5. MONOLITHIC BEDS TESTING

This chapter presents the test bench which has been build to test the efficiency of the monolithic beds described in chapter 2.

The main features of this bench are described, along with the testing procedures which have to be followed when using highly concentrated solutions of hydrogen peroxide.

Finally, the outcome of the experimental activity is summarized.

5.1 Description of the test bench

The main components of the experimental apparatus are:

- the hydrogen peroxide tank (volume: ~2 litres);
- the injector;
- the catalytic chamber.

All the components are made of stainless steel.

The core of the bench is the catalytic chamber, whose schematic drawing is reported in the Annex A: it is a stainless steel cylinder, with a length of 65mm and a maximum diameter equal to 60mm.

The cylinder is hollow, to allow the insertion of monolithic beds up to 60mm in length and 13mm in width; a certain number of thermocouples (up to eight) can be inserted in the holes distributed along the chamber axis: in this way, the experimental characterization of the temperature profiles along the monolithic bed is possible.

A picture of the catalytic chamber (equipped with thermocouples) is shown in Fig. 47.
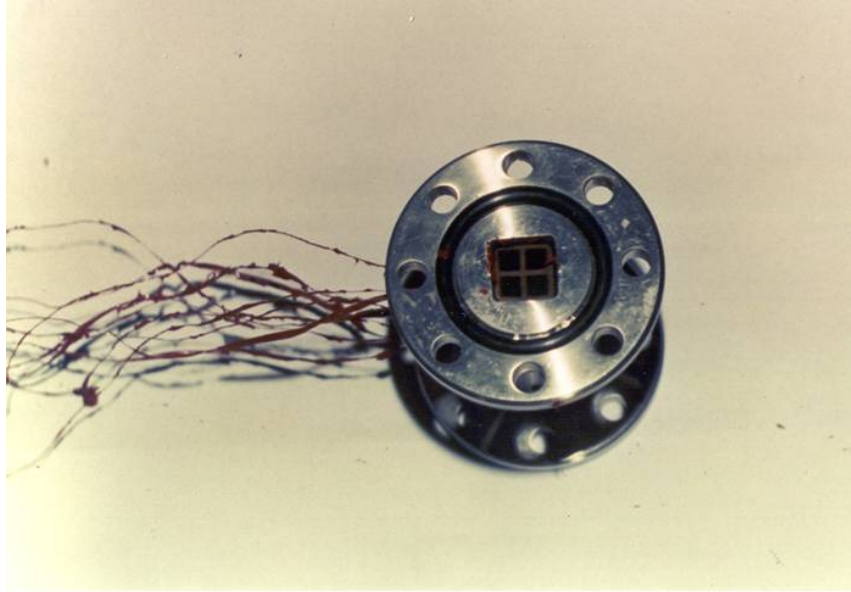
Figure 47. Catalytic chamber (note the monolithic bed inside the stainless steel support)

The modular structure of the bench should be pointed out: in the present configuration, tests at atmospheric pressure and in mono-propellant configuration are possible; nevertheless, a nozzle can be easily added to the catalytic chamber outlet, to vary the operating pressure; in a similar way, a simple cylindrical vessel containing a solid fuel can be connected to the outlet, in order to perform hybrid firing tests (bi-propellant configuration).

Further details on the experimental apparatus can be found in [46].

5.2 Testing procedures

Before any test can be performed, all the components which will be in contact with the peroxide solution are treated according to the following procedures, which are necessary to avoid any undesired decomposition of the peroxide before it arrives in the catalytic reactor (i.e. in the tank and in the feeding lines):

- degreasing: its main purpose is to eliminate any trace of impurity (as oil, grease etc.) from the surface exposed to the peroxide flow; it basically consists in washing such surfaces with a warm solution of bi-distillate water in which sodium salts have been dissolved;

- pickling, to remove any oxide film due to welding and previous thermal treatments of the metallic components;

- passivation, to promote the formation of a oxide film which improves the chemical stability of the metallic surfaces.

Further details on the above procedures can be found in [46].

At the beginning of each test, the tank is pressurized up to the value which corresponds to the desired mass flow rate: as no flow regulator is mounted on the line between the tank and the injector, such flow rate will not be constant, but will decrease as long as the pressure in the tank decreases. This is the main drawback of any blow-down pressurization system: anyway, if the volume of the peroxide used during each firing is small compared to the tank volume (as in the tests carried out in the present work), such pressure variation is small too and a constant mass flow rate can be assumed.

The pressure in the tank is continuously monitored by means of a pressure transducer: the need for such transducer arises not only for the reasons explained above, but also to record any pressure increase due to early hydrogen peroxide decomposition in the tank.

The signals from the pressure transducer and from the thermocouples are processed via a dedicated Labview software.

The hydrogen peroxide solution which has been used in the present work has a 60% weight grade: the choice of such solution is mainly due to safety issues.

At this concentration, the decomposition temperature remains below the boiling point, hence no transition from the liquid phase to the vapour phase can be observed. For this reason, the flow inside the monolithic bed will be different from the one expected with more concentrated solutions and described in the previous chapters. Anyway, the results of the tests with a 60% weight hydrogen peroxide solution give fundamental information about the activity and the stability features of the catalytic reactor.

The monolithic beds (support: cordierite, active phase: manganese dioxide) have been previously described in chapter 2: the main geometrical features are reported in Tab. 37.

Table 37. Geometrical features of the monolithic beds used in the present work

Length, mm	30
Channel dimension, mm	5
Cross section shape	Square

5.3 Results

The hydrogen peroxide solution flow rate has been fixed to about $4.4 \cdot 10^{-3}$ kg/s: two test series have been performed. Five thermocouples have been mounted on the catalytic chamber: unfortunately, only the measurements of two sensors have been considered reliable.

As shown in Fig. 48, in the first test the temperature remains approximately constant for about 50s (the origin of the x-axis is not set to zero because of a shift between the starting of the acquisition and the opening of the valve which allows the peroxide to flow from the tank to the catalytic chamber).
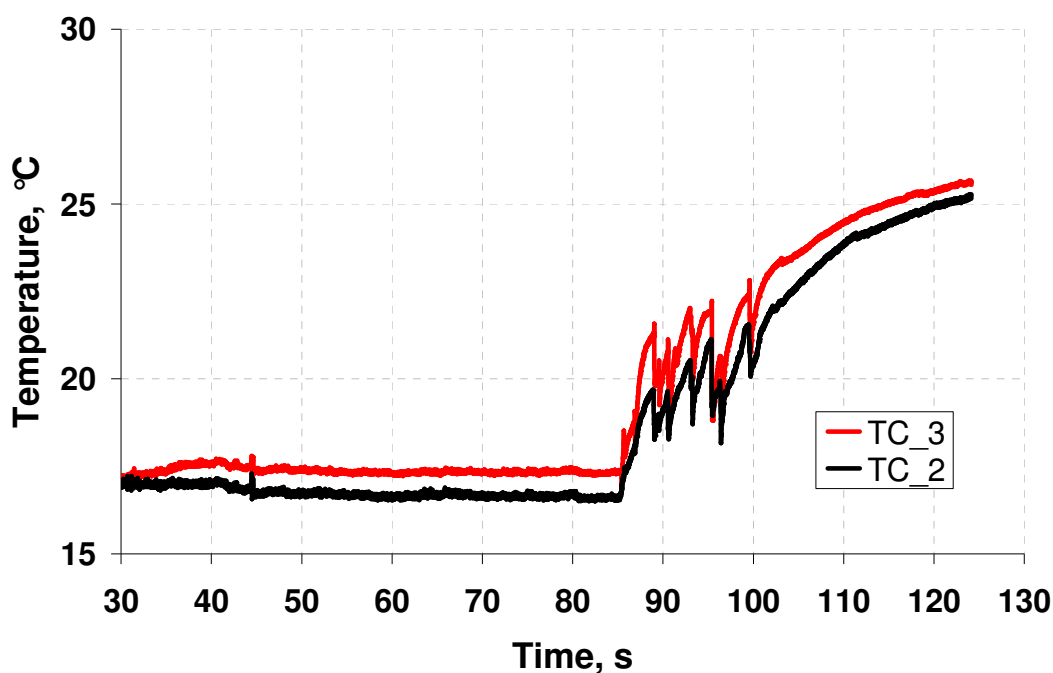
Figure 48. Temperature time history (test #1)

After this induction period, the temperature increases up to 26°C: such value is smaller than the one corresponding to a full decomposition of a 60% weight hydrogen peroxide solution (about 94°C, starting from the initial temperature of 16°C recorded in the experiments).

In the second test series, the activity of the catalytic bed is much reduced, as can be inferred from Fig. 49, which shows an almost constant temperature profile: according to these results, the monoliths seem to have a short operating life, limited to about 200s.
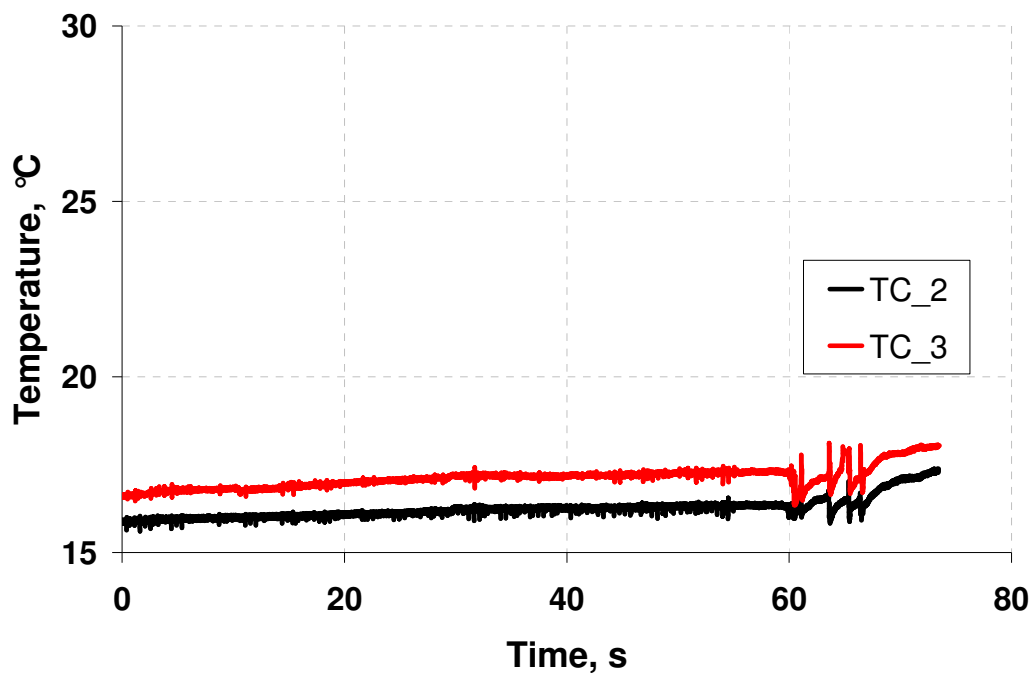
Figure 49. temperature time history (test #2)

This behaviour is not coherent with the high catalyst stability which has been experimentally observed during the tests with the batch reactor, summarized in chapter 2: during such tests, continuous activity of the cordierite-based monoliths up to 8000s has been recorded.

New tests with the batch reactor, using the same catalyst and the same hydrogen peroxide solution, have been carried out in order to fix the problem: poor performances (with respect to both the catalyst activity and stability) have been measured in the constant-volume configuration too.

As no change in the preparation procedure of the monolithic beds had occurred, the cause of this different behaviour has been supposed to be the hydrogen peroxide solution: proper analyses of the solution composition have demonstrated that the peroxide used in the last phase of the present work has an amount of stabilizers much higher than the solution used during the early tests, though the supplier had been the same and no variation in the nominal composition had been reported by the supplier itself.

6. CONCLUSIONS AND FUTURE WORKS

The hydrogen peroxide has a strong potential as a propellant in space propulsive systems, for both high-thrust and low-thrust level applications.

The peroxide-based propulsion has reached a very high technology readiness level in the past and several applications have been developed up to flight operations: among the others, the British launchers Black Knight and Black Arrow deserve a special mention. After the big step towards a H_2O_2 propulsion represented by the successful launch of such vehicles in the early Seventies, the peroxide faded out and other propellants, as the cryogenic liquid hydrogen and liquid oxygen and the non-cryogenic but highly toxic hydrazine and nitrogen tetroxide, have powered almost every space vehicle.

Starting from the end of the Nineties, new requirements and new applications have been moving more and more attention towards the return of the hydrogen peroxide in space engines. Among the others, the following issues are leading the peroxide revolution:

- cost reduction;

- environmental impact reduction;

- miniaturization of the thrust generation systems.

As reported in the first chapter of this work, the hydrogen peroxide can in principle successfully address the above issues: anyway, due to the lack of expertise and know-how during the peroxide "dark age" in the last thirty years and to brand new requirements which should be fulfilled (for example on micro-thrusters scale), several technological challenges need to be overcome before a H_2O_2-powered system can fly again.

Most of the work to be done is related to the development of a reliable and efficient catalytic chamber, able to convert the chemical energy stored in the H_2O_2 molecule into thermal energy: the most appealing feature of the peroxide as propellant is actually its ability to decompose into hot gases (water and oxygen), whose thermal energy can be directly converted into mechanical energy through the expansion in a nozzle to generate the desired thrust level (mono-propellant configuration) or used to start the ignition and the combustion of a proper fuel (solid or liquid) without any auxiliary power source (bi-propellant configuration).

The hard job related to the development of the catalytic chamber has been reported in chapter 2: starting from the many drawbacks related to the technological solutions (i.e. packed beds) which have been traditionally employed in space applications, a new configuration has been selected in

the present work. It basically relies on the utilization of monolithic beds, very similar to the ones massively used for chemical and automotive applications: both new materials and new preparation procedures and techniques have been employed in the development of such beds. The extensive activity which has been performed to experimentally characterize the catalysts has highlighted the following points:

- the developed catalysts show a high activity, comparable with the values which have been reported in literature for similar systems;

- the hydrogen peroxide decomposition starts at low (ambient) temperature too: the importance of this result for the practical application to space propulsive systems is straightforward, because it guarantees the possibility to ignite the engine without additional ignition devices, whose power and mass requirements negatively affect the engine performances; other mono-propellants which are currently under investigation in the scientific community (i.e. HAN blends) do not exhibit a similar behaviour and require a high catalyst temperature to start the decomposition reaction;

- a high catalyst stability has been recorded: this result has been achieved using commercial-grade hydrogen peroxide solutions, which usually have a stabilizers content much higher than the one used for the propulsive-grade solutions; as the stabilizers act as a poison, binding to the active sites on the catalytic surface and progressively causing a loss of activity, the developed catalysts have proved to be able to successfully withstand an operating environment harder than the one which correspond to the real application in space engines, at least with respect to the chemical stability;

- a novel technique has been applied to prepare the catalytic beds: such technique eliminates the intermediate layer (referred to in literature as washcoat), which is usually added to increase the catalysts surface area (as the reaction occurs at the solid/fluid interface, the advantage related to a high interface area are straightforward); the following considerations are worthwhile:

  o as stated above, the catalysts developed in the present work have shown a catalytic activity comparable with the values reported in literature, despite the lower surface area due to the absence of the washcoat layer;

  o a high resistance to the thermal shocks associated with the ignition/shut down cycles of the engine should result from the absence of the intermediate layer: the material which is commonly used as washcoat (i.e. the alumina) does experience phase transitions when subjected to thermal cycling and such transitions can cause damages to the catalyst structure with a loss of active area and finally the reactor failure.

87

Once the basic features of the catalyst have been experimentally assessed, a theoretical/numerical methodology has been developed, in order to support the design of the monolithic reactor to be used in a real H_2O_2-based engine. To the author's knowledge, such design has widely relied upon experimental testing and only very few attempts to identify general design guidelines, able to reduce the time and the cost associated to empirical or semi-empirical procedures, have been reported in literature. Furthermore, such attempts have been focused on completely different configurations: for example, a packed bed has been investigated in [47], while modelling and simulation of the hydrogen peroxide decomposition in micro-channels have been addressed in [48, 49] for MEMS-scale devices.

Starting from the analogies between the reactor configuration selected for the present work and the one used in other industrial applications (i.e. in the automotive sector), the modelling assumptions and strategies adopted to design and analyse the flow in the catalytic converters commonly used on ground vehicles have been selected as a base-line.

A lumped-parameters (or 1-D) model has been then developed: the comparison with experimental data available in literature and with the predictions of more detailed numerical tools (i.e. CFD simulations) has proved that such model is able to correctly reproduce the most important features of the physical and chemical processes occurring in the reactor and hence to correctly evaluate the reactor performances. In particular, the model predicts with reasonable accuracy the time response of the catalytic chamber: as outlined more than once in this work, the unsteady behaviour of the catalyst is extremely important, because it determines the control capabilities of the propulsion system. Moreover, the position of the ignition point, i.e. the point along the monolithic bed where the temperature jumps almost instantaneously to the final adiabatic value (as expected for a solid/gas heterogeneous reaction in a adiabatic reactor, see chapter 3) can be estimated with reasonable accuracy too. A correct evaluation of the ignition point is essential to achieve a correct sizing of the catalytic chamber.

The 1-D tool does operate almost in real-time: it can be used to screen several different configuration and to evaluate the impact of different design variables (among the others: peroxide flow rate, peroxide grade, inlet temperature, shape and size of the monolithic channel, catalyst activity) in a very short time. No similar results can be achieved by means of experimental testing, because a wide screening activity just relying on empirical procedures would be very expensive and time-consuming; in a similar fashion, CFD-based techniques can not be widely used to support such screening, due to the high computational effort required by each CFD simulation.

The experimental and numerical work which has been developed in the present thesis forms the basis for further developments, whose final aim is to increase the technology readiness level of hydrogen peroxide-based propulsion systems.

The following considerations can be regarded as guide-lines for future works.

On the experimental side:

- testing the developed monolithic beds using propulsive-grade H_2O_2 solutions is of course a fundamental step towards a full assessment of their potential;

- further testing using lab-scale operating conditions is still necessary to achieve a complete characterization of the catalyst activity and stability: as a large fraction of the real reactor will operate in vapour phase and as the ignition does occur once the solution has completely vaporized (as demonstrated in chapter 4), a thorough experimental assessment of the hydrogen peroxide decomposition in vapour phase is essential; further practical advantages are related to such tests, since the stabilizers added to the peroxide solutions do not vaporize and hence no poisoning of the catalyst should be expected (as a consequence, the problems which have been faced in the present work when dealing with highly stabilized commercial grade solutions should not occur); a dedicated bench for the analysis of the catalytic decomposition of vaporized hydrogen peroxide has been build and preliminary tests are on-going;

- due to the high cost of the propulsive-grade peroxide, the possibility to have a *in loco* production of highly concentrated solutions should be carefully assessed.

On the theoretical/numerical side:

- the developed lumped-parameters model can be extended to include the effect of other processes which are supposed to have a strong influence on the reactor performances, with particular attention to the response time and to the position of the ignition point; as explained in chapter 3, the present model does not include the effect of axial conduction, for both the gas and the solid phase; the possibility to assess the influence of the solid thermal conductivity can identify alternative paths to more efficient catalysts (for example metallic monoliths);

- further comparison with CFD simulations is also advantageous, both to support the development of the simplified model and to analyse the fluid/structure interaction within the catalytic chamber.

The following consideration about future developments of the present work is worthwhile: in the last years, several groups have started to work on hydrogen peroxide-based propulsion all around Europe: a closer and stronger cooperation among these groups would be strongly advantageous.

REFERENCES

[1] F.Sietzen Jr., The greening of rocket, *Aerospace America*, July 2005, 28-35

[2] M. Ventura and P. Mullens, "The use of hydrogen peroxide for propulsion and power", AIAA Paper 99-2880

[3] A.J. Musker, Personal communication, 3rd International Conference on Green Propellants for Space Propulsion, Poitiers, september 2006

[4] E.J. Wernimont, "Monopropellant hydrogen peroxide rocket systems: optimum for small scale", AIAA Paper 2006-5235

[5] A.J. Musker, J.J. Rusek, C: Kappenstein and G.T. Roberts, "Hydrogen Peroxide: from Bridesmaid to Bride", Proceedings of the 3rd International Conference on Green Propellants for Space Propulsion, ESA-SP-635, 2006

[6] A.D.Ketsdever and J.Mueller, "Systems Considerations and Design Options for Microspacecraft Propulsion Systems", AIAA Paper 99-2723

[7] http://lisa.jpl.nasa.gov/

[8] D.L. Hitt, C.M. Zakrzwski and M.A. Thomas, MEMS-based satellite micropropulsion via catalyzed hydrogen peroxide decomposition, *Smart Materials and Structures* 10, 1163-1175, 2001

[9] Schumb W.C., Satterfield C.N., Wentworth R.L., *Hydrogen peroxide*, Reinhold Publishing Company, New York, 1955

[10] A. Buri and A. Marotta, *Chimica. Lezioni per gli studenti delle Facoltà di Ingegneria*, Liguori Editore, Napoli, 1987

[11] A. J. Musker and G.T. Roberts, "An Exploratory Study of Some Liquid Catalysts for Use with Hydrogen Peroxide", Proceedings of the 3rd International Conference on Green Propellants for Space Propulsion, ESA-SP-635, 2006

[12] S. Bonifacio, Utilizzazione del perossido di idrogeno nei sistemi propulsivi spaziali, Tesi di Laurea, Università degli Studi di Napoli Federico II, Napoli, 2002

[13] J.J.Sellers, Investigation into cost-effective propulsion systems for small satellites, Ph.D. Thesis, University of Surrey, 1996

[14] A. Cybulski and J.A.Moulijn, *Catal.Rev.-Sci.Eng.*, 36 (2), 179-270, 1994

[15] T.Beutien, S.Heister, J.Rusek and S.Meyer, "Cordierite-Based Catalytic Beds for 98% Hydrogen Peroxide", AIAA Paper 2002-3853

[16] C.Scharlemann, M.Schiebl, K.Marhold, M.Tajmar, P.Miotti, C.Kappenstein, Y.Batonneau, R.Brahmi, C.Hunter, "Development and Test of a Miniature Hydrogen Peroxide Monopropellant Thruster", AIAA Paper 2006-4550

[17] S.Barley and P.L.Palmer, "Evaluating the Miniaturization of a Monopropellant Thruster", AIAA Paper 2006-4549

[18] S. Irandoust and B. Andersson, Monolithic Catalysts for Non-Automobile Applications, *Catal. Rev.-Sci. Eng.*, 30 (3), 341-392, 1988

[19] J.J. Rusek, New decomposition catalysts and characterization techniques for rocket-grade hydrogen peroxide, *Journal of Propulsion and Power*, Vol. 12 No. 3, 574-579, May-June 1996

[20] M. A. Hasan, M. I. Zaki, L. Pasupulety and K. Kumari, Promotion of the hydrogen peroxide decomposition activity of manganese oxide catalysts, *Applied Catalysis A: General* 181, 171-179 (1999)

[21] L. Pirault-Roy, C. Kappenstein, M. Guerin, R. Eloirdi and N. Pillet, Hydrogen peroxide decomposition on different catalsts. Effect of stabilizer, *Journal of Propulsion and Power*, Vol. 18 No. 6, 1235-1241, November-December 2002

[22] A.Russo Sorge, M.Turco, G.Pilone, G.Bagnasco, Decomposition of Hydrogen Peroxide on MnO_2/TiO_2 Catalysts, *Journal of Propulsion and Power*, Vol. 20, No. 6, 1069-1075, November-December 2004

[23] R. Palmieri, Catalizzatori a base di ossido di manganese su zirconia per la decomposizione del perossido di idrogeno, Tesi di Laurea, Università degli Studi di Napoli Federico II, Napoli, 2004

[24] T. Onori, Tesi di Laurea, Università degli Studi di Napoli Federico II, Napoli, 2004

[25] C. Bramanti, A. Cervone, L. Romeo, L. Torre, L. D'Agostino, A.J. Musker and G. Saccoccia, "Experimental characterization of advanced materials for the catalytic decomposition of hdyrogen peroxide", AIAA Paper 2006-5238

[26] H.S.Fogler, Elements of Chemical Reactor Engineering, 2nd Edition, Prentice-Hall, 1992

[27] N.Gupta and V.Balakotaiah, Heat and mass transfer coefficients in catalytic monoliths, *Chemical Engineering Science* 56 (2001) 4771-4786

[28] R.H.Heck, J.Wei, J.R.Katzer, Mathematical Modeling of Monolithic Catalysts, *AIChE Journal* (Vol. 22 No.3), May 1976, 477-484

[29] W.M.Kays, *Convective Heat and Mass Transfer*, McGraw-Hill Book Company, 1966

[30] S. Gordon & B. J. Mc Bride, "Computer program for calculation of complex chemical equilibrium compositions and applications; ii. users manual and program description", NASA RP 1311, 1996

[31] R. C. Reid, J. M. Prausnitz and B. E. Poling, *The properties of gases and liquids*, 4th Edition, McGraw-Hill, New York, 1987

[32] C.N.Satterfield and F.P.Audibert, Nucleate and film boiling in the catalytic decomposition of hydrogen peroxide, *I&EC Fundamentals*, Vol. 2 No. 3 august 1963, 200-202

[33] H.D.Baehr, K.Stephan, N.J.Park, *Convective heat and mass transfer. flows with phase change*, in Heat and Mass Transfer, Springer-Verlag 1998

[34] L. B. Datsevich, Some theoretical aspects of catalyst behaviour in a catalyst particle at liquid (liquid-gas) reaction with gas production: oscillation motion in the catalyst pores, *Applied Catalysis A: General* 247, 2003, 101-111

[35] L.B.Datsevich, Alternating motion of liquid in catalyst pores in a liquid/liquid-gas reaction with heat or gas production, *Catalysis Today* 79-80, 2003, 341-348

[36] R.J Kee, G. Dixon-Lewis, J. Warnatz, M.E. Coltrin and A. J. Miller, "A Fortran computer code package for the evaluation of gas-phase multicomponent transport properties", Sandia National Laboratories Report SAND86-8246 (1986)

[37] W.H. Press, B.P. Flannery, S.A. Teukolsky, W.T. Vetterling, *Numerical Recipes in FORTRAN: the art of scientific computing*, 2nd Edition, Cambridge University Press (MA), 1992

[38] R. Taylor and R. Krishna, Multicomponent Mass Transfer, Wiley, New York, 1993

[39] K. Sutton and P.A. Gnoffo, Multi-component diffusion with application to computational aerothermodynamics, AIAA Paper 98-2575

[40] H.J. Merk, The macroscopic equations for simultaneous heat and mass transfer in isotropic, continuous and closed systems, *Appl. Sci. Res.*, 8:73-99, 1958

[41] Fluent 6.0 User's Guide, Fluent Inc., Lebanon (NJ), 2001

[42] R.K.Edvinsson Albers, M.J.J.Houterman, T.Vergunst, E.Grolman and J.A.Moulijn, Novel Monolithic Stirred Reactor, *AIChE Journal* Vol. 44 No. 11, November 1998, 2459-2464

[43] L.C.Young and B.A.Finlayson, Mathematical Models of the Monolith Catalytic Converter, *AIChE Journal* Vol. 22 No. 2, March 1976, 331-353

[44] H. Schlichting, *Boundary Layer Theory*, 7th Edition, McGraw-Hill, 1979

[45] S.Z. Barley, P.L. Palmer, J.R. Wallbank and A.M. Baker, "Characterisation of a Monopropellant Microthruster Catalytic Bed", AIAA Paper 2005-4544

[46] V.Di Matteo, Progetto e realizzazione di un banco prova per la misura dell'efficienza di catalizzatori monolitici per la decomposizione del perossido di idrogeno, Tesi di Laurea, Università Federico II, Napoli, 2006

[47] L.M. Chiappetta, L.J. Spadaccini, H. Huang, W. Watkins and A.M. Crocker, "Modeling a Hydrogen Peroxide Gas Generator for Rockets", AIAA Paper 2000-3223

[48] X. Zhou and D.L. Hitt, "One-Dimensional Modeling of Catalyzed H_2O_2 Decomposition in Microchannel Flows", AIAA Paper 2003-3584

[49] X. Zhou and D.L. Hitt, "Numerical Modeling of Monopropellant Decomposition in a Micro-Catalyst Bed", AIAA Paper 2005-5033

[50] T. Zhang, "Catalyst Design and Catalytic Process for Space Propulsion", Proceedings of the 3rd International Conference on Green Propellants for Space Propulsion, ESA-SP-635, 2006
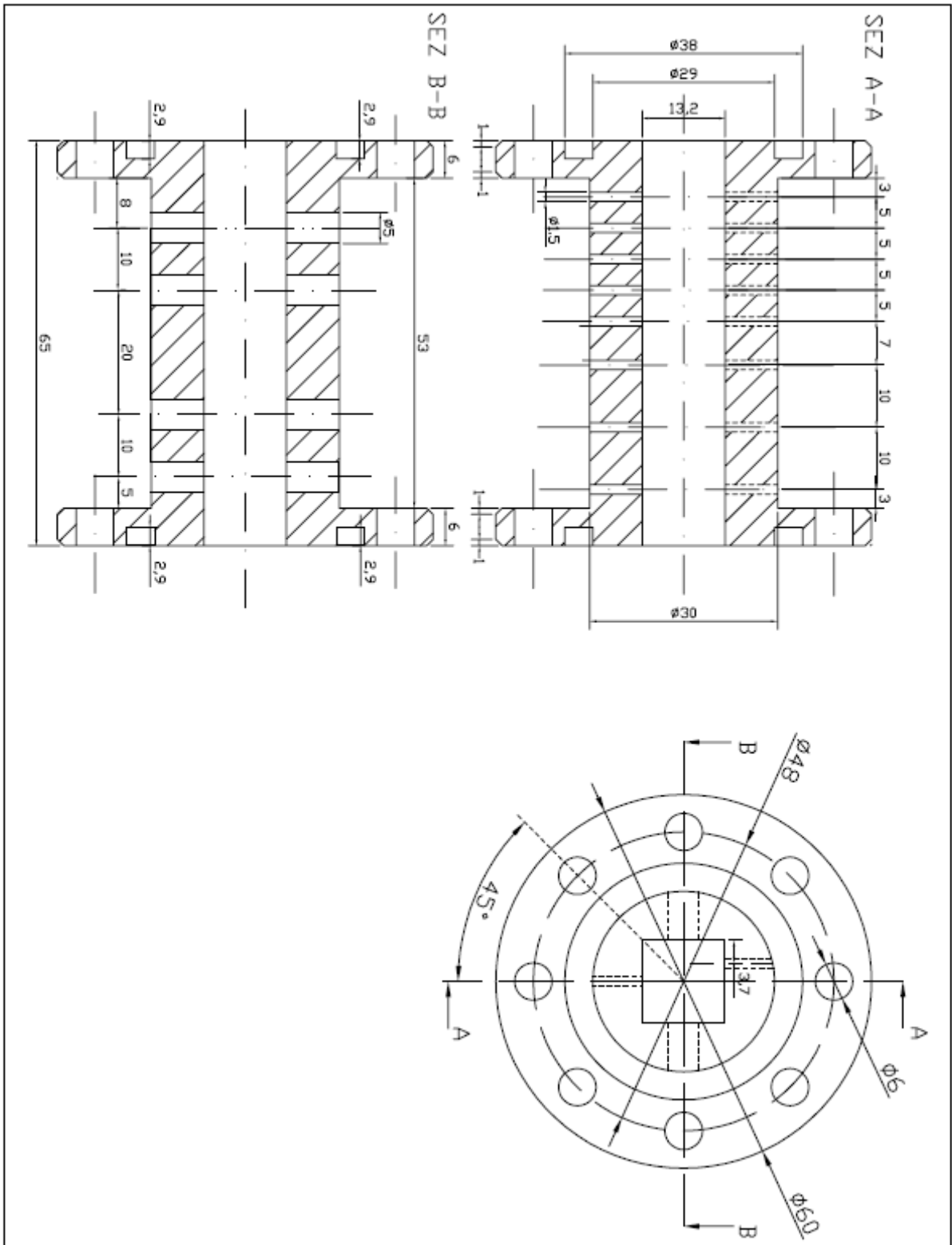
ANNEX A

Figure 50. Schematic drawings of the chamber developed in the present work to evaluate the performances of monolithic beds